

Spatial Confinement Approach Using Ni to Modulate Local Carbon Supply for the Growth of Uniform Transfer-Free Graphene Monolayers

Cheng-Yu Dai, Wei-Chun Wang, Chi-Ang Tseng, Fang-Chi Ding, Yit-Tsong Chen, and Chiao-Chen Chen*

Cite This: *J. Phys. Chem. C* 2020, 124, 23094–23105

Read Online

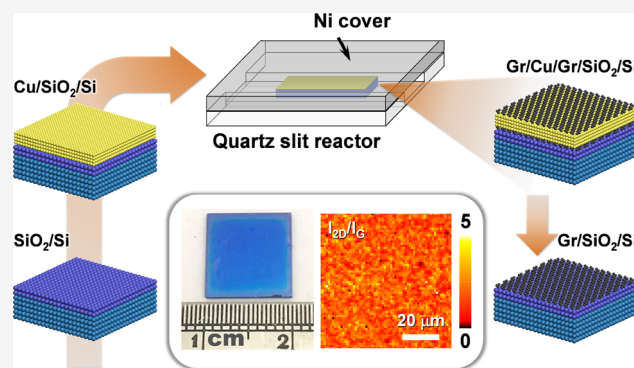
ACCESS |

Metrics & More

Article Recommendations

Supporting Information

ABSTRACT: Direct growth of high-quality graphene on dielectric substrates without a sophisticated transfer process is one of the key challenges to effectively integrate graphene synthesis with the existing semiconductor manufacturing process. In this study, we take advantages offered by a customized reactor to realize the synthesis of uniform transfer-free graphene monolayers on SiO₂/Si substrates via the metal-catalytic chemical vapor deposition method. The optimal reactor is designed to be a Ni-covered quartz slit with a confined reaction space (length × width × height = 85 × 13 × 0.55 mm³). The slit structure of this reactor offers a spatially confined environment for effectively suppressing Cu evaporation and modulating the growth kinetics of graphene. In addition, the Ni cover serves as a carbon absorbent for regulating the local concentration of carbon species within the slit reactor, which increases the monolayer content of the produced graphene. With the optimal synthesis protocol, transfer-free graphene with low defects and high monolayer content (>90%) was prepared directly on SiO₂/Si substrates as continuous large-area films (1 × 1 cm²) or microscale patterns with sheet resistance and field-effect mobility of 334 Ω/sq and 962 cm²/(V s), respectively.



1. INTRODUCTION

Graphene, which was the first isolated two-dimensional nanomaterial,^{1,2} is considered to be a promising replacement for silicon in the semiconductor industry because of its unique electrical, optical, and flexibility properties.^{3,4} Chemical vapor deposition (CVD) is one of the most reliable processes for the mass production of high-quality large-area graphene. However, CVD reactions for graphene synthesis commonly require the use of catalytic metal substrates on which graphene formation is initiated.⁵ Consequently, an additional process is required to transfer the produced graphene from the catalytic metal to dielectric substrates for subsequent device fabrication. Unfortunately, conventional transfer processes, such as polymer-assisted,^{6,7} tap-assisted,⁸ and polymer-free^{9–13} transfer, inevitably introduce defects and contaminations in graphene, which deteriorate the graphene quality. By contrast, the direct synthesis of graphene on a target substrate considerably simplifies the graphene preparation process by eliminating laborious and sophisticated transfer steps. Consequently, the production cost in terms of time and labor can be considerably reduced. Moreover, the direct synthesis method avoids the polymer residues, cracks, folding, and other defects frequently introduced by conventional transfer processes; thus, the production of high-quality graphene is

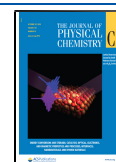
ensured. The direct growth of transfer-free graphene on silica substrates facilitates the integration of graphene synthesis with the existing complementary metal–oxide–semiconductor technology; thus, the potential of graphene in various industrial applications is enhanced.

Transfer-free graphene has been directly grown on dielectric substrates without using metallic catalysts.^{5,14–21} However, without the use of powerful metallic catalysts, the production of large-scale and high-quality graphene is challenging because of harsh synthesis conditions, such as elevated temperature (>1425 °C),^{21,22} prolonged growth time (approximately 5–72 h),^{5,23} and ultrahigh vacuum (10^{−10} Torr).^{19,20} Another method that is promising for preparing transfer-free graphene involves depositing metal films on target substrates and then growing graphene at the metal–substrate interface through a CVD process. The deposited metal film is subsequently etched

Received: June 10, 2020

Revised: September 13, 2020

Published: October 13, 2020



away to leave the synthesized graphene directly on the dielectric substrate.^{24–38} With this process, some studies have achieved the formation of large-area, transfer-free graphene in the laboratory scale (i.e., 1–4 cm in edge length)^{27,28,30,34,35} or in the wafer scale (i.e., 5–10 cm in diameter).^{25,31,32} In addition, transfer-free graphene patterns with a desired geometry can be produced at defined locations on a target substrate using a patterned metal film without an elaborate post-growth photolithographic process.^{39–42} Such a preparation has not been realized in metal-catalyst-free graphene synthesis.

Although the aforementioned pioneering studies indicate the considerable potential of using deposited metal films to grow transfer-free graphene, except the works reported by the Lu's and the Di's group,^{32,38} most graphene produced in them were multiple layered, lack of uniformity, without controllable dimensions and/or with inadequate electrical properties, as presented in Table S1. In other words, reliable methods to synthesize transfer-free graphene monolayer with high uniformity for both large-area films and defined patterns are still limited. For the uniform deposition of graphene using CVD method, well-controlled fluidic dynamics in the reaction system is believed to be crucial⁴³ and a confined reaction environment has been demonstrated to benefit the growth of large graphene single crystals on Cu foils.^{44,45} Herein, we attempted to exploit a spatial confinement approach for preparing uniform transfer-free graphene using deposited Cu films on SiO₂/Si substrates in a customized reactor. This reactor comprised a quartz slit with a confined reaction space and a Ni cover as the carbon absorbent. Within the spatially confined reaction space, where Cu evaporation was considerably suppressed and the local carbon concentration was regulated by the Ni absorbent, high-quality transfer-free graphene with a monolayer content >90% was successfully prepared to form continuous films (1 × 1 cm²) and microscale patterns with defined geometries (circles, squares, and hexagons with characteristic lengths of 20–300 μm).

2. EXPERIMENTAL SECTION

2.1. Preparation of Catalytic Metal Films on SiO₂/Si Substrates.

For directly growing transfer-free graphene on a dielectric substrate via low-pressure CVD (LPCVD) method, catalytic metal films were deposited on a Si substrate with a 300 nm thick thermal SiO₂ layer through ion-beam sputter coating (Commonwealth Scientific IBS250). Prior to the deposition of metal films, a 4-in. SiO₂/Si wafer (thickness, 525 μm) was cut into pieces with dimensions of 1 × 1 cm². These pieces were cleaned with acetone for 10 min in an ultrasonic bath, rinsed with isopropyl alcohol and deionized water, and then blow-dried with nitrogen gas. The cleaned 1 × 1 cm² SiO₂/Si substrates were then sputter-coated with metal films for graphene synthesis. To obtain uniform metal films with high purity, the sputtering process was conducted in high vacuum at an Ar pressure of 7.6 × 10⁻³ Torr with a deposition rate of 0.8 Å/s for Cu (99.999% purity) and 0.4 Å/s for Ni (99.999% purity). The deposited metal films with various thicknesses (i.e., 400–1000 nm) and Ni/Cu compositions (i.e., Ni/Cu ratio = 0, 5, and 10%) were examined. Patterned transfer-free graphene was also synthesized in this study. For this purpose, SiO₂/Si substrates with desired photoresist patterns were developed through a conventional photolithography process, followed by the sputter deposition of metal films and a lift-off process for removing the photoresist.

The aforementioned process enabled the creation of patterned metal films on the SiO₂/Si substrates.

2.2. CVD Growth of Transfer-Free Graphene.

Transfer-free graphene was synthesized in an LPCVD system with a reaction chamber constructed by a 1-in. quartz tube (wall thickness of 0.1 cm) and a split-tube furnace (Thermo Scientific, Lindberg Blue M) with a heating zone of 10 cm. In the tubular reaction chamber, a customized quartz slit reactor (Figures 1b and 2b) with a confined space to accommodate

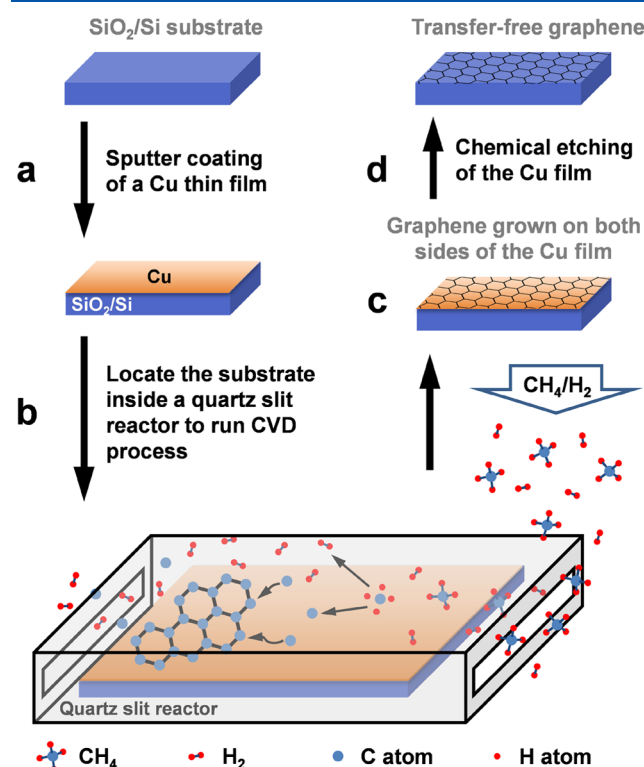


Figure 1. Procedure for preparing transfer-free graphene on SiO₂/Si substrates in a spatially confined reactor. (a) A SiO₂ (300 nm thick)/Si substrate was first sputter-coated with a Cu thin film (thickness, 400–1000 nm). (b) Cu/SiO₂/Si substrate was placed within the quartz slit reactor for the CVD synthesis of graphene. (c) Graphene grew on the upper Cu surface and at the Cu–SiO₂ interface. (d) Transfer-free graphene grown at the Cu–SiO₂ interface was exposed through chemical etching of the Cu film using 0.1 M ammonium persulfate (APS).

the metal/SiO₂/Si substrate was utilized to grow transfer-free graphene. With the quartz slit reactor, synthesis conditions, including the chamber pressure, reaction temperature, annealing time, growth duration, reactant composition, reactor configuration, and metal-film composition, were investigated systematically (Table S2).

3. RESULTS AND DISCUSSION

The steps of the process adopted in this study for growing transfer-free graphene are displayed in Figure 1. In brief, a Cu film was first deposited onto a SiO₂/Si substrate. The Cu/SiO₂/Si substrate was placed inside a quartz slit reactor, which was then inserted into the heating zone of a tubular furnace to conduct the CVD process. The transfer-free graphene grown at the Cu–SiO₂ interface in the CVD process was then exposed by etching the metal film with 0.1 M ammonium persulfate (APS). We believed that the quartz slit reactor ensured the

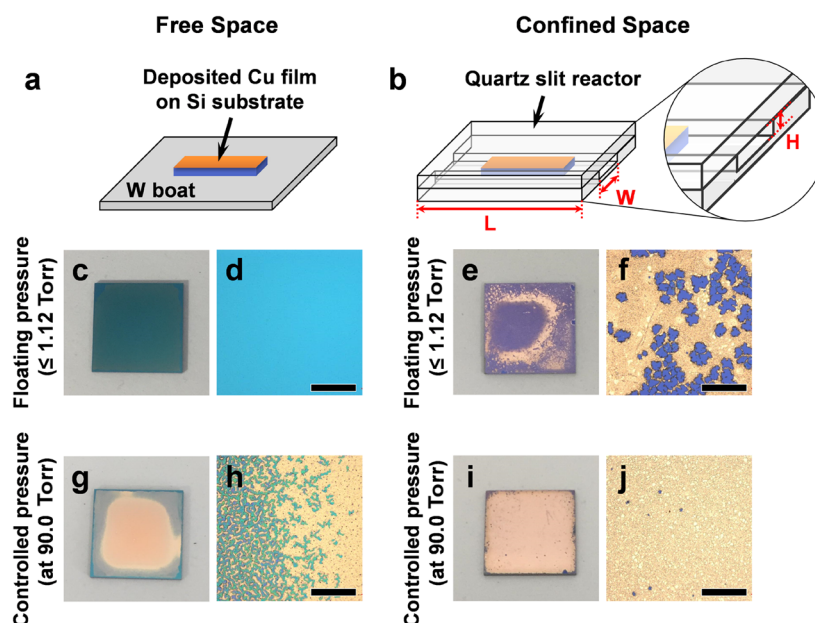


Figure 2. Two reactor configurations and optical images of the as-synthesized samples before the chemical etching of Cu. (a) Cu/SiO₂/Si substrate was placed on a tungsten (W) boat and exposed to the reaction gas directly. (b) Cu/SiO₂/Si substrate was located inside a quartz slit reactor with a confined space (length × width × height = 85 × 13 × 0.65 mm³). Photographs (c, e, g, i) and optical micrographs (d, f, h, j) of the 1 × 1 cm² Cu (400 nm thick)/SiO₂/Si substrate that underwent a complete CVD process without special control of the chamber pressure (c–f) and under a controlled reaction pressure of 90.0 Torr (g–j). Scale bars: 200 μm.

integrity of the metal film over the Si substrate during the entire CVD process, which enabled the formation of continuous graphene films. This assumption was confirmed by comparing the integrity of Cu films after performing the CVD process with two distinct reactor configurations (Figure 2).

In the conventional CVD system (Figure 2a), the Cu/SiO₂/Si substrate with a 400 nm thick Cu film was placed on a tungsten (W) boat, which was located in a free reaction space defined by the quartz tubular chamber. The substrate underwent a typical CVD process (Table S2, P0) at 1000 °C without special control of the chamber pressure, which remained <1.12 Torr. Consequently, because of the low pressure and the elevated temperature close to the melting point of Cu at 1084 °C, considerable sublimation and dewetting of the Cu film occurred over the entire substrate (Figure 2c). On the Si substrate, even small Cu residues were barely observed with an optical microscope (Figure 2d). By contrast, for the CVD system with a quartz slit reactor (Figure 2b) inside the tubular chamber, a confined reaction space (85 × 13 × 0.65 mm³) was established to accommodate the Cu/SiO₂/Si substrate. When using the aforementioned synthesis parameters except the CVD system comprising a confined reaction space (Table S2, P1), the evaporation of copper was effectively suppressed, as indicated by a notable Cu film remaining on the substrate (Figure 2e,f).

This phenomenon can be attributed to the significant decrease in the flow velocity within a confined space, which effectively reduces the sublimation rate of Cu.⁴⁵ Furthermore, the space restriction imposed by the slit reactor tends to shift the kinetic equilibrium of the sublimated Cu atoms from escape into the carrier gas (Ar, which is continuously vacuumed out during the CVD process) toward redeposition onto the Si substrate. Therefore, the experimental design with a confined space allows an intact Cu film to be maintained

throughout the CVD process. An intact Cu film is a prerequisite for preparing a continuous graphene film because the graphene synthesized via metal-catalytic CVD is typically limited within the area covered by the catalytic metal.⁴⁶ To improve the coverage of the Cu film, the chamber pressure was controlled at 90.0 Torr (upper limit of the LPCVD system utilized in this study) for graphene growth (Table S2, P10). Under a controlled pressure of 90.0 Torr, a confluent Cu film (Figure 2i) with only a few pinholes (Figure 2j) was obtained within the confined reaction space. By contrast, notable dewetting of the Cu film (Figure 2g,h) could not be avoided with the conventional experimental setup associated with a free reaction space.

To successfully prepare uniform and large-area transfer-free graphene, the CVD parameters which could influence the growth mechanisms of graphene were systematically investigated using the slit reactor. Figure 3a displays the commonly accepted mechanisms for the metal-catalytic CVD synthesis of graphene. In general, the growth process begins from the dissociative chemisorption of methane to generate carbon adatoms (Figure 3a,i). These active carbon species may (1) increase the carbon concentration until local supersaturation to initiate graphene nucleation (Figure 3a,ii), (2) diffuse along the Cu surface to attach existent carbon clusters for graphene enlargement (Figure 3a,iii), or (3) escape from the upper surface of Cu through thermal desorption (Figure 3a,iv). Graphene formation is also observed at the Cu–SiO₂ interface. In this case, carbon adatoms formed on the upper surface of Cu are believed to transport through bulk diffusion (Figure 3a,v) or diffusion across the grain boundaries of Cu (Figure 3a,vi) and then reach the metal–dielectric interface where carbon crystallizes to form graphene.^{25,47} Considering the aforementioned mechanisms, using the reactor configuration illustrated in Figure 2b (i.e., the slit reactor with a quartz cover and a gap size of 0.65 mm), crucial CVD parameters were

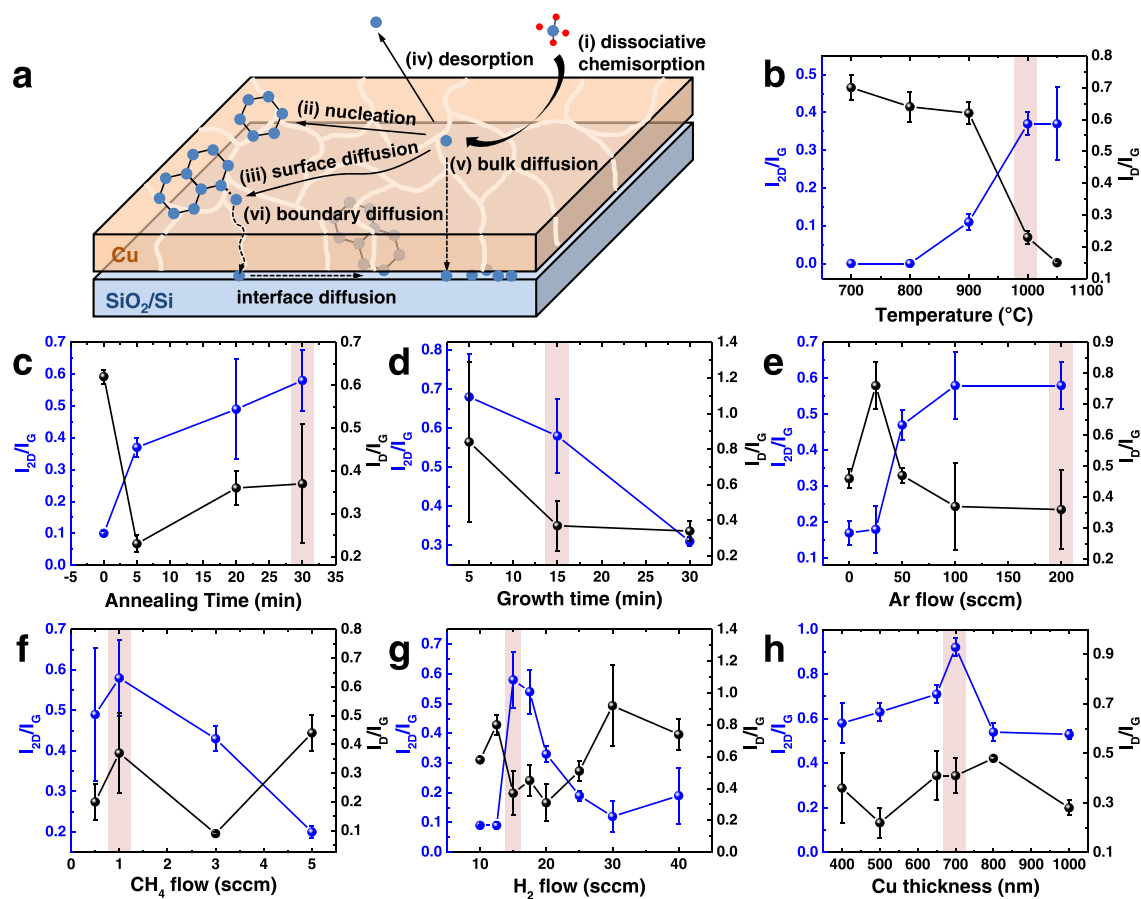


Figure 3. (a) Schematic illustrates the formation mechanisms of graphene on both sides of the deposited Cu film: (i) dissociative chemisorption of CH₄, (ii) graphene nucleation due to local supersaturation of carbon atoms, (iii) surface diffusion, (iv) thermal desorption, (v) bulk diffusion of carbon adatoms, and (vi) grain boundary diffusion of carbon adatoms. To optimize the synthesis protocol, the influence of CVD parameters, including the (b) growth temperature, (c) annealing duration, (d) growth time, (e) Ar flow rate, (f) CH₄ flow rate, (g) H₂ flow rate, and (h) Cu film thickness, on the quality of the produced graphene was investigated systematically in terms of the I_{2D}/I_G and I_D/I_G ratios determined from Raman measurements. The data points obtained from the optimal setting of each parameter are marked by red strips.

selected for detailed examination, as described in Section 2 of the Supporting Information (Figures 3 and S1; Table S2, P2–P26).

The quality of the produced graphene was systematically investigated by plotting the ratios of I_{2D}/I_G and I_D/I_G as functions of the synthesis parameters under study, as displayed in Figure 3b–h, in which the optimal conditions resulting in graphene with the highest I_{2D}/I_G ratio (i.e., thinnest thickness) and an acceptable I_D/I_G ratio <0.4 (i.e., limited defects) are marked with red strips. Considering the page limitation and not to distract the focus of this report too much, detailed discussions about how we select the optimal synthesis parameters are moved to Section 2 of the Supporting Information for the interested audiences. With the optimized conditions of temperature, annealing time, growth duration, and reactant compositions (P10 in Table S2), confluent transfer-free graphene with a thickness of three to five layers (estimated from an I_{2D}/I_G ratio of 0.58)⁴⁸ was obtained. To further reduce the thickness of the produced graphene to a monolayer, different strategies were adopted for adjusting the carbon concentrations at the Cu–SiO₂ interface. These strategies included (1) increasing the thickness of Cu films to reduce the rate of carbon deposition in the vertical direction through bulk and grain boundary diffusion, (2) reducing the gap size of the slit reactor to suppress the internal flow rate and

thus modify the kinetics of graphene growth, and (3) replacing the quartz cover of the slit reactor with a Ni plate as a carbon sink to absorb excessive carbon species.

To evaluate the relationship between the quality of the produced graphene and the thickness of the Cu films, the effect of various Cu film thicknesses (from 400 to 1000 nm) was investigated (Table S2, P10, and P27–P31). Raman characterization (Figures 3h and S1h) indicated that increasing the Cu film thickness from 400 to 700 nm did result in the formation of a thinner graphene film, as demonstrated by the increased I_{2D}/I_G ratio. This result can be attributed to the extended vertical mass transport pathway of carbon through the bulk and grain boundaries of Cu (Figure 3a,v,vi), leading to a decrease in the carbon concentration at the Cu–SiO₂ interface under a constant growth time. However, when the Cu film thickness was increased to 800 nm, the thickness of graphene increased. Although the vertical transport of carbon can be suppressed by a thick Cu film, the total amount of dissolved carbon in Cu is suspected to increase with the mass of the deposited Cu film. Consequently, for a thick Cu film, the precipitation of dissolved carbon during the cooling stage of a CVD process might thicken the produced graphene film. Although graphene growth catalyzed by Cu is commonly accepted to involve a surface-limited mechanism rather than a dissolution–precipitation process because of the low carbon solubility of Cu,⁴⁹ it

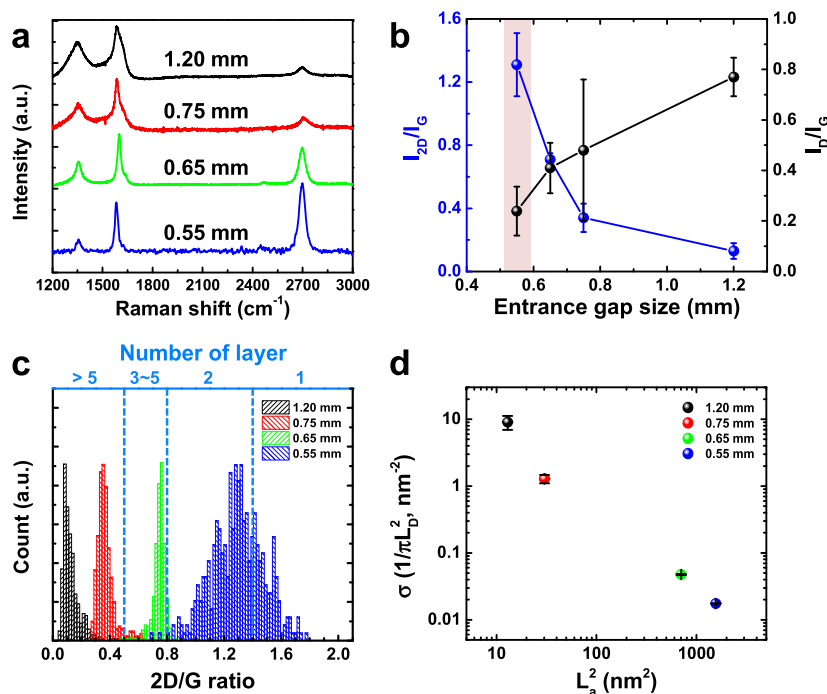


Figure 4. With the other synthesis parameters being unchanged, quality improvement of the produced graphene by reducing the gap size of the slit reactor from 1.20 to 0.55 mm was verified from (a) representative Raman spectra and (b) statistical analysis of the recorded I_{2D}/I_G and I_D/I_G ratios. (c) The I_{2D}/I_G ratios of graphene obtained from slit reactors with different gap sizes are illustrated as histograms to identify the difference in the layer number of graphene. (d) The density of point defects (σ) and the crystallite area (L_a^2) estimated for each sample indicated that the structural defects decreased notably with the gap size of the slit reactor.

has been reported that the carbon solubility in nanometer-sized Cu vapor, which is sublimated from Cu foil at elevated temperature, is comparable to that in bulk Ni.⁵⁰ Furthermore, the redeposition of these carbon-rich Cu droplets is facilitated by covering the Cu foil with a quartz cap (similar to the confined space utilized in this study) for promoting the transport of carbon feedstock from Cu vapor to bulk Cu. Consequently, the coverage of the produced graphene film was increased.⁵⁰ Therefore, we believe that the competition between reducing the vertical carbon transport and increasing the amount of carbon feedstock is a function of the Cu film thickness, which must be limited within a certain range dominated by reducing the vertical diffusion for producing graphene monolayers. Consequently, Cu/SiO₂/Si substrates with 700 nm thick Cu films were utilized for subsequent graphene synthesis.

Because the Cu film thickness does not have a monotonic influence on the graphene thickness, we attempted to enable the formation of monolayer graphene by modifying the configuration of the slit reactor. The effect of the confined reaction space on the graphene quality was investigated using slit reactors with four gap sizes ranging from 1.20 to 0.55 mm, as displayed in Figure 4 (Table S2, P29 and P32–P34). Raman measurement demonstrated that the graphene film synthesized with the smallest gap size (0.55 mm) had the highest quality among the synthesized graphene films, as indicated by its high I_{2D}/I_G ratio and low I_D/I_G ratio (Figure 4a,b). Detailed analyses of 400-point Raman spectra for samples synthesized with different gap sizes were conducted. Considering that many factors, such as defects, strain, and substrates,^{51–53} could affect the Raman spectra of graphene and the graphene produced here did display a relatively higher amount of defects, the following Raman criteria^{26,32,54,55} are applied to

determine the graphene layer number. For the monolayer graphene with structural disorders,⁵⁶ it is generally accepted to have an I_{2D}/I_G ratio of >1.4 and a broadening full width at half maximum of 2D band (Γ_{2D}) ranging between 24 and 45 cm⁻¹. (More detailed discussion about the Raman criteria of monolayer graphene can be found in Section 3 of the Supporting Information.) For bilayer graphene, the Raman criteria are set to be 0.8–1.4 for the I_{2D}/I_G ratio and 45–61 cm⁻¹ for the Γ_{2D} . For graphene samples with an I_{2D}/I_G ratio of <0.8 and a Γ_{2D} of >61 cm⁻¹, the number of layers is estimated to be >3 . The I_{2D}/I_G ratios obtained for the samples in this study are illustrated as histograms in Figure 4c. When the gap size was reduced from 1.20 to 0.55 mm, the average I_{2D}/I_G ratio increased from 0.13 to 1.29, which indicated that the graphene thickness significantly reduced from more than five layers to no more than two layers.^{26,32,54,55}

The amount of structural defects in the produced graphene was evaluated from the density of point defects ($\sigma = 1/\pi L_D^2$, where L_D is the average distance between point defects)^{53,56,57} and the crystallite area (L_a^2 , where L_a is the average distance of line defects).^{57,58} Both the aforementioned parameters can be estimated from the I_D/I_G ratios or the full width at half maximum of the G band (Γ_G). The Raman spectra displayed in Figure 4a indicates that the produced graphene samples had a relatively broad Γ_G range (approximately 22.5–82.5 cm⁻¹). The Γ_G values of these samples were higher than 15 cm⁻¹, which is a characteristic Γ_G value for graphitic materials with fairly limited structural defects.^{57,59} Thus, the graphene samples obtained here possessed a relatively high amount of structural defects. Consequently, the density of point defects (σ) and the crystallite size (L_a) could not be estimated appropriately with the following well-known equations using I_D/I_G ratios:^{53,58}

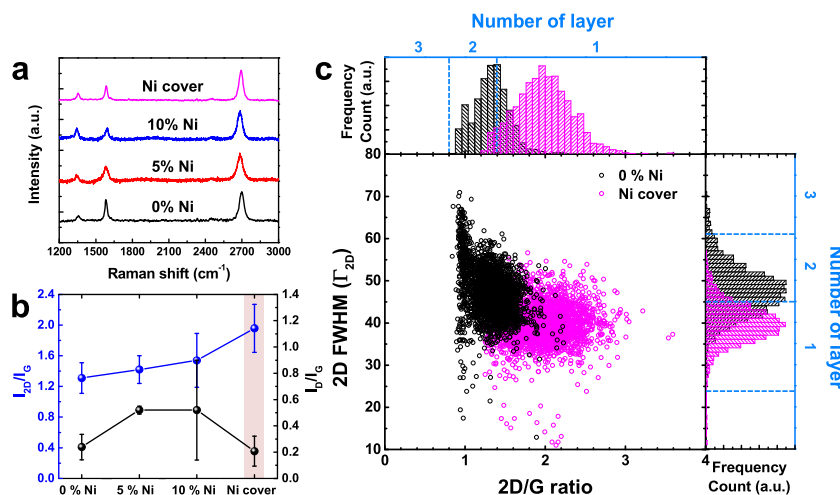


Figure 5. Nickel was utilized to regulate the layer number of the produced graphene by designing four types of catalyst substrates for CVD synthesis: (1) 0% Ni: pure Cu (700 nm thick) films, (2) 5% Ni: Cu (665 nm thick, lower)/Ni (35 nm thick, top) films, (3) 10% Ni: Cu (630 nm thick, lower)/Ni (70 nm thick, top) films; all of the aforementioned substrates were located in a pure quartz silt reactor, and (4) Ni cover: pure Cu (700 nm thick) films inside a slit reactor with a Ni cover. (a) Raman spectra and (b) the corresponding I_{2D}/I_G and I_D/I_G ratios of the graphene prepared using the aforementioned four types of substrates demonstrated that the application of Ni is beneficial for the formation of monolayer graphene. (c) Statistical analysis of >2000 Raman spectra of the graphene produced using the 0% Ni and Ni cover substrates indicated an overall shift toward increased I_{2D}/I_G ratios and reduced Γ_{2D} values for the graphene obtained with the Ni cover substrates.

$$\sigma \text{ (nm}^{-2}\text{)} = 1/\pi L_D^2 = \frac{E_L^4}{4300\pi} \left(\frac{I_D}{I_G} \right) \quad (1)$$

where E_L is the laser energy.⁵³

$$L_a \text{ (nm)} = \frac{560}{E_L^4} \left(\frac{I_D}{I_G} \right)^{-1} \quad (2)$$

which is known as the Tuinstra–Koenig–Cançado relation.⁵⁸ Alternatively, by fitting the recorded Γ_G values to the reported relationship shown in Figure S5c, which describes Γ_G as a function of L_D and L_a ,^{56,57} the density of point defects ($\sigma = 1/\pi L_D^2$) of the graphene samples decreased by approximately 3 orders of magnitude and the crystallite area (L_a^2) increased by approximately 2 orders of magnitude as the gap size of the slit reactor reduced from 1.20 to 0.55 mm (Figure 4d). The distinct reduction in the structural defects was attributed to decreased mass transport (diffusion) of reactants onto the Cu substrate through a fluid boundary (stagnant) layer, which was significantly thickened because of reduced gas velocity within the confined reaction space.^{45,60} The suppressed mass transport of carbon in the confined space decreased the carbon deposition rate, which reduced the graphene nucleation density. The decrease in the carbon deposition rate and graphene nucleation density suppressed the formation of structural defects. Consequently, graphene with improved crystallinity can be obtained with a spatially confined reactor.

When the gap size of the slit reactor was 0.55 mm, the produced graphene possessed a monolayer content of approximately 35% and a bilayer content of approximately 65% (Figure S6a,b). To further improve the uniformity of graphene, we introduced Ni into the system to promote the formation of monolayer graphene through the modulation of the local carbon concentration within the slit reactor. Nickel, which is another frequently used catalytic metal in graphene synthesis, displays high carbon solubility at elevated temperature and thus is believed to induce the formation of graphene through a dissolution–precipitation mechanism.⁶¹ Therefore, a

sufficiently slow cooling speed is required to precipitate the dissolved carbon in the bulk of Ni out on its surface for graphene growth.^{6,62,63} In addition, it has been proved that Ni can serve as an effective carbon absorbent to spatially regulate the nucleation and layer numbers of synthesized graphene.^{64,65} According to these pioneering studies, we attempted to facilitate the growth of uniform monolayer graphene by exploiting the absorption ability of Ni for excess carbon and by limiting carbon precipitation through a rapid cooling speed for freezing the dissolved carbon inside the bulk Ni.

In this part of experiments, four types of metal/SiO₂/Si substrates were investigated (Figure S7): (1) 0% Ni: pure Cu films with a thickness of 700 nm; (2) 5% Ni: metal films composed of a 650 nm thick Cu (lower layer) and a 35 nm thick Ni (top layer); (3) 10% Ni: metal films composed of a 630 nm thick Cu (lower layer) and a 70 nm thick Ni (top layer); all of the aforementioned three types of substrates were located within a pure quartz slit reactor; and (4) Ni cover: 700 nm thick pure Cu films inside a slit reactor with its quartz cover replaced by a Ni plate. For the metal films composed of Cu and Ni, a Cu–Ni alloy formed during the annealing step to catalyze subsequent graphene growth.^{63,66,67} The Raman measurements indicated that the average I_{2D}/I_G ratio increased from 1.31 to 1.54 as the Ni composition increased from 0 to 10%, which implied evident enhancement in the monolayer content of the produced graphene (Figure 5a,b and Table S2, P32 and P35–P37). However, despite the increase in the I_{2D}/I_G ratios, the graphene prepared with metal films containing Ni exhibited structural deterioration, demonstrated by the increased I_D/I_G ratios. This result can be attributed to that a significant amount of carbon was absorbed by Ni, which not only reduced the graphene thickness but also increased the graphene defects by reducing graphene grain size and suppressing the formation of a continuous graphene film. Large fluctuations in the I_{2D}/I_G and I_D/I_G ratios for the graphene prepared from metal films with 10% Ni implied that the continuity of the produced graphene was restricted (Figure 5b). In addition, graphene exhibits a stronger interaction with

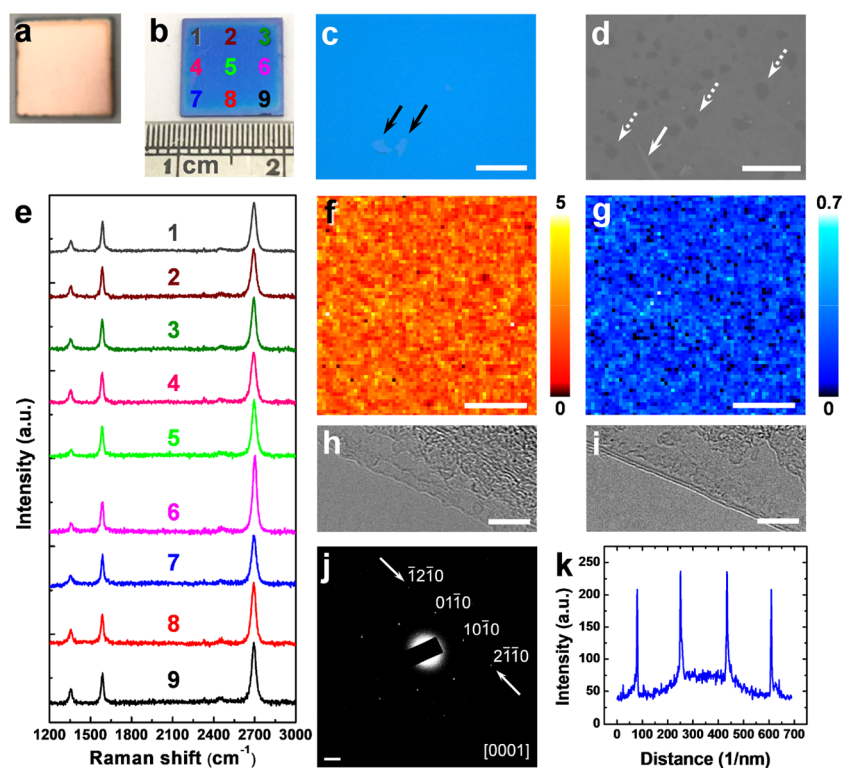


Figure 6. Photographs of an as-synthesized sample (a) before and (b) after the chemical etching of the Cu film. (c) Optical micrograph and (d) scanning electron microscopy (SEM) image of the sample displayed in (b) revealed only a few tears (black arrows) and cracks (white solid arrow) on the produced transfer-free graphene. The dark spots (white dash arrows) in the SEM image indicated the existence of bilayer graphene. (e) Raman spectra recorded from nine different positions marked in (b) as well as the ratios of (f) I_{2D}/I_G and (g) I_D/I_G demonstrated that the synthesized graphene had a low number of defects and high uniformity. The high-resolution transmission electron microscopy (HR-TEM) images indicated the presence of both (h) monolayer and (i) bilayer edges on the produced graphene. (j) Selected area electron diffraction (SAED) pattern of the monolayer region displays a hexagonal symmetry. (k) A line profile of the diffraction peak intensities along the white arrows shown in (j). Scale bars: (c) 40 μm , (d) 1 μm , (f, g) 20 μm , (h, i) 5 nm, and (j) 2 nm^{-1} .

Ni than with Cu;⁶⁸ thus, completely removing Ni or Ni alloys from graphene through chemical etching by APS is difficult. Consequently, considerable contamination of Ni residues was observed on the produced transfer-free graphene (Figure S8d); this contamination may have contributed to graphene defects.

Therefore, to use Ni as an effective modulator for local carbon supply without introducing the contamination of residual Cu–Ni alloys, we replaced the quartz cover of the slit reactor (gap size of 0.55 mm) with a Ni plate as a local carbon sink that did not have physical contact with the deposited Cu film. By adopting this strategy, the contamination of the residual Cu–Ni alloy was avoided and the average I_{2D}/I_G ratio of the produced graphene increased to 1.96, with its I_D/I_G ratio remaining at 0.21 (Figure 5b). The Raman analysis results for the graphene synthesized from pure Cu films using a slit reactor with a quartz cover (denoted as 0% Ni) and a slit reactor with a nickel cover (denoted as Ni cover) are illustrated in Figure 5c. A clear overall shift toward increased I_{2D}/I_G ratios and reduced Γ_{2D} values was observed, which confirmed the decrease in the graphene layer number. According to the aforementioned Raman criteria (i.e., an I_{2D}/I_G ratio of >1.4 and a Γ_{2D} value of approximately 24–45 cm^{-1} for monolayer graphene), transfer-free graphene with a monolayer coverage of >90% was obtained using the slit reactor with a Ni cover (Figure S6c,d).

When using the optimal synthesis protocol (Table S2, P37), the Cu/SiO₂/Si substrates undergoing a complete CVD process displayed a uniform Cu surface without notable

dewetting (Figure 6a). In addition, we did observe Raman signals of graphene films from the top surface of deposited Cu (Figure S9b). Although the Raman analysis of this upper-layer graphene was obscured by the background signal from the photoluminescence of underlying Cu,^{69,70} the thickness of this graphene film appeared to be no more than two layers with an average I_{2D}/I_G ratio of ~ 1.2 . To verify the growth of transfer-free graphene at the Cu–SiO₂ interface, we applied a two-step etching process (Figure S9a). With this process, we can ensure there are no residual graphene films formed on the upper surface of deposited Cu to be landed onto the silica substrate during the etching of the Cu film and thus prevent the ambiguous source of produced transfer-free graphene. Since it took about 15 min to completely remove a 700 nm thick Cu film using 0.1 M APS, the two-step etching process was designed to be 3 and 12 min for the first and the second etching stage, respectively. After the first etching step was done, at least five locations over a 1 \times 1 cm^2 substrate were examined by Raman measurement (Figure S9c), which demonstrated that only amorphous carbon with a broad G band was detected instead of well-crystallized graphene with sharp G and 2D bands. The background signal from Cu fluorescence remained notable indicating that only the outermost Cu surface was removed while the bulk of the Cu film still maintained. Therefore, the amorphous carbon was detected in the bulk of the Cu film, confirming the vertical diffusion of active carbon species in the Cu film, which is a

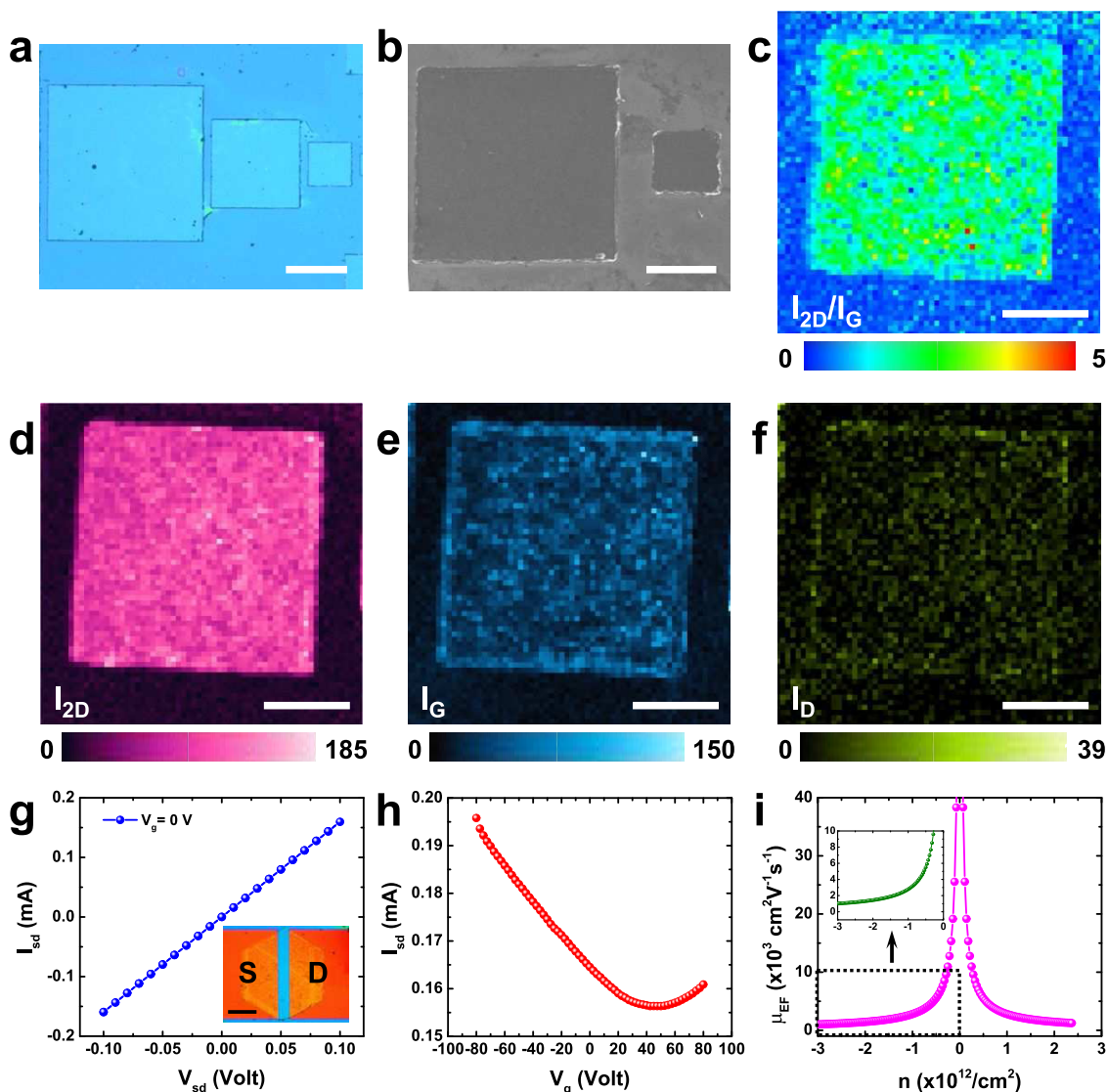


Figure 7. (a) Optical micrograph and (b) SEM image of the synthesized graphene patterns. Raman mappings for the (c) I_{2D}/I_G ratio as well as the intensities of the (d) 2D, (e) G, and (f) D peaks of a representative graphene square with a $60\ \mu\text{m}$ edge. (g) $I_{sd}-V_{sd}$ curves of the graphene field-effect transistor (GFET) at $V_g = 0\ \text{V}$. The inset displays the contrast-enhanced optical micrograph of a representative GFET (S: source and D: drain) made from a hexagonal pattern (Figure S12c,d) with a conducting channel having dimensions of $112 \times 14\ \mu\text{m}^2$. (h) Representative transfer curve with V_{Dirac} at $47\ \text{V}$. (i) Relationship between the μ_{eff} and n values derived from the experimental data. The inset displays an enlargement of the data region marked with a dashed rectangle. Scale bars: (a) $40\ \mu\text{m}$, (b–f) $20\ \mu\text{m}$, and the inset of (g) $35\ \mu\text{m}$.

critical process for the growth of transfer-free graphene at the Cu–SiO₂ interface as mentioned in Figure 3a.

After the complete removal of the Cu film via the second etching step, the transfer-free graphene grown at the Cu–SiO₂ interface was exposed to show well-characterized G and 2D bands with an I_{2D}/I_G ratio of ~ 2.3 (Figure S9d). The photograph of a representative $1 \times 1\ \text{cm}^2$ SiO₂/Si substrate covered with a confluent transfer-free graphene layer is displayed in Figure 6b. In this figure, no significant color contrast can be identified by naked eyes, implying that a graphene film with uniform coverage was obtained. The optical micrograph and scanning electron microscopy (SEM) image (Figure 6c,d) of the synthesized graphene sample confirmed that it had limited morphological defects. The sample only had a few tears (Figure 6c, black arrows) and cracks (Figure 6d, white solid arrow). The dark spots (Figure 6d, white dashed arrows) in the SEM image, which have a diameter of $\leq 250\ \text{nm}$,

are regarded as bilayer graphene, which was estimated to have $<10\%$ coverage in the graphene sample. This result is consistent with the estimation from the Raman measurements. Figure 6e displays the Raman spectra for nine positions on the sample displayed in Figure 6b. The nine positions exhibited outstanding spectral consistency, which demonstrated the structural uniformity of the synthesized graphene. The Raman spectra in Figure 6e exhibit the characteristic peaks of graphene at $\sim 1355\ \text{cm}^{-1}$ for the D band, $\sim 1578\ \text{cm}^{-1}$ for the G band, and $\sim 2695\ \text{cm}^{-1}$ for the 2D band. The relative intensities of these peaks agree well with the reported values for low-defect graphene monolayers.⁷¹ Two-dimensional Raman mapping was performed over a randomly selected area of $75 \times 75\ \mu\text{m}^2$ for the sample displayed in Figure 6b. Mappings of the I_{2D}/I_G (Figure 6f) and I_D/I_G (Figure 6g) ratios were analyzed to have an average value of 1.96 ± 0.31 (where $I_{2D}/I_G \geq 1.4$ for $>90\%$ of the data points) and 0.21 ± 0.11 , respectively. The spectral

consistency between the point measurements and the two-dimensional Raman mappings verified the structural homogeneity of the produced graphene in the micrometer and centimeter scales. Furthermore, to obtain explicit evidence regarding the crystallinity and thickness of the produced graphene, transmission electron microscopy (TEM) characterizations were performed. Using a conventional polymer-assisted transfer process, the graphene synthesized on SiO₂/Si substrates was transferred onto a lacey-carbon-coated TEM grid. The high-resolution TEM (HR-TEM) images indicated that the synthesized graphene had monolayer (Figure 6h) and bilayer edges (Figure 6i), which is consistent with the Raman characterizations. The selected area electron diffraction (SAED) pattern within the monolayer region exhibited a typical hexagonal symmetry of graphene (Figure 6j). The {1100} spots were more intense than the {2110} spots by a factor of approximately 1.2 (Figure 6k), which implied that the graphene sample had monolayer characteristics.⁷² In addition, a number of ripples, tears, and folds (Figure S10a) were introduced in the graphene film because of the imperfect transfer process, which may lead to random twisting angles or disoriented stacking configurations and thus resulted in the generation of multiple sets of SAED patterns (Figure S10b).⁷³ To further confirm the thickness of transfer-free graphene films, atomic force microscopy (AFM) was applied to obtain the height profiles of produced graphene (Figure S11). From both the AFM and the corresponding optical microscopic images (Figure S11a,c), folds of the transfer-free graphene were found at the edge of the 1 × 1 cm² Si substrate where the detachment of the graphene film from the Si substrate frequently occurred during the etching process of Cu films using a solution-based etchant. From the recorded line profiles (Figure S11b), the heights of produced graphene range between 0.76 and 0.88 nm with an average of 0.83 ± 0.05 nm, consistent with the reported monolayer characteristic of graphene on SiO₂/Si substrates.^{5,74–76}

Batch fabrication of transfer-free graphene patterns with a characteristic dimension of 20–300 μm was realized using the synthesis strategy reported in this study. In this study, patterned Cu films (Figure S12a,c) with a thickness of 700 nm were deposited on SiO₂/Si substrates through a conventional photolithography process. The optimal synthesis protocol (Table S2, P38) was performed with these substrates to obtain transfer-free graphene patterns having well-defined geometries (including microscale circles, squares, and hexagons), which perfectly duplicated the Cu patterns observed in the optical microscopy and SEM images (Figure 7a,b for square patterns and Figure S12 for all three patterns). Raman mapping was performed for a representative graphene square with a 60 μm edge to examine its spatial uniformity. The intensity maps of the I_{2D}/I_G ratio and the 2D, G, and D bands (Figure 7c–f) indicated that the graphene pattern had high structural homogeneity. In addition, the statistical analyses of >2000 Raman spectra obtained through two-dimensional mapping (illustrated as histograms in Figure S13a–f) indicated that the I_{2D}/I_G was 1.90 ± 0.32 (where I_{2D}/I_G ≥ 1.4 for approximately 95% of the data points), Γ_{2D} was 39.3 ± 2.8 cm⁻¹, the I_D/I_G ratio was 0.31 ± 0.09, and Γ_G was 21.7 ± 1.3 cm⁻¹, which suggested that the graphene pattern represented a highly uniform monolayer.

Finally, the electrical properties of the transfer-free graphene, namely, the sheet resistances and field-effect mobility, were examined under vacuum (~2 × 10⁻³ Torr) at room

temperature. Using a conventional four-point probe method, the average sheet resistance of the continuous graphene films covering the entire 1 × 1 cm² SiO₂/Si substrate was determined to be 334.4 ± 112.3 Ω/sq, which is higher than the values obtained in most of the studies listed in Table S1. In addition, graphene field-effect transistors (GFETs) were fabricated from the graphene patterns by a routine process reported in our previous study (Section 4 of the Supporting Information).⁴⁵ Briefly speaking, to fabricate GFETs, metal contacts were deposited over graphene patterns via thermal evaporation using a TEM grid as the shadow mask. After the device fabrication, the existence of metal contacts significantly obscured the visualization of the underlying graphene as shown in the recorded optical micrograph (Figure S14b). To improve the visibility of the underlying graphene in GFETs, imaging parameters of the charge-coupled device (CCD) camera, including brightness, γ nonlinearity, and the color saturation, were adjusted accordingly. Consequently, the contrast-enhanced micrograph of a representative GFET made from a hexagonal graphene pattern was obtained (inset of Figures 7g and S14c). The dependence of the source–drain currents (I_{sd}) on the source–drain voltages (V_{sd}) at zero gate voltage (V_g) is shown in Figure 7g, which represents a perfect ohmic response with a linear I–V relationship and negligible leakage current (<10 pA). Figure 7h illustrates the transfer curve recorded for a representative GFET at V_{sd} = 0.1 V. This transfer curve exhibited considerable p-doping, which is attributed to adcharges from SiO₂ defects (such as oxygen-rich dangling bonds) and/or admolecules (such as water or hydrocarbons from the air) trapped on the graphene surface or at the graphene–SiO₂ interface.^{77–79} The transfer curve, which describes I_{sd} as a function of V_g, can be utilized to evaluate the device resistance (R_{tot}), metal–graphene contact resistance (R_{contact}), and graphene channel resistance (R_{channel}). By fitting the experimental data with eq S1 (Supporting Information), R_{contact} was determined to be 363.2 Ω. This value was then subtracted from R_{tot} to determine R_{channel}. The channel resistivity (ρ), which was calculated from R_{channel} by the following equation: ρ = R_{channel} × (W/L), where W is the channel width and L is the channel length, was utilized to determine the field-effect mobility (μ_{ef} = 1/nερ, where n is the carrier density and e is the elementary charge). The field-effect mobility (μ_{ef}) was then plotted as a function of the carrier density n (n = C_g(V_g – V_{Dirac})/e, where V_{Dirac} is the Dirac point at 47 V and C_g = 11.5 nF/cm² is the capacitance for the 300 nm thick SiO₂ layer), as displayed in Figure 7i. This plot indicated that μ_{ef} was >5300 cm²/(V s) when n < 5 × 10¹¹ cm⁻². Moreover, μ_{ef} approached a limit of 962 cm²/(V s) at n = 3 × 10¹² cm⁻², which corresponded to a large (V_g – V_{Dirac}) value at ±42 V, at which the mobility of the GFET was dominated by Coulomb-impurity scattering for monolayer graphene.

4. CONCLUSIONS

In this paper, we reported a practical method for preparing high-quality transfer-free graphene directly on SiO₂/Si substrates using a reactor with a slit configuration. Because of the spatially confined environment offered by the slit reactor, the sublimation of Cu thin films, which is a problem inevitably encountered in LPCVD process for graphene synthesis, was effectively suppressed. Consequently, the

integrity of Cu films was maintained throughout the entire CVD process, which allowed the formation of large-area transfer-free graphene in the laboratory regime. The gap size of the slit reactor, which affects the quality of the produced graphene by modifying its growth kinetics, could be easily tuned to adapt to substrates with different thicknesses for preparing uniform and low-defect graphene films. Furthermore, a Ni plate, which served as an effective remote carbon absorbent, was utilized as the cover of the slit reactor to modulate the local carbon concentration within the reactor. The use of a Ni plate led to the successful synthesis of transfer-free graphene with a monolayer content of >90% and without nickel contamination. Using a patterned Cu film, graphene patterns with desired geometry at the micrometer scale could be accurately created at defined positions on a Si substrate. Consequently, the graphene synthesis process adopted in this study is highly compatible with the silicon-based integrated-circuit technology for the mass production of graphene-based devices. The prepared graphene displayed adequate electrical properties, with a sheet resistance of 334 Ω /sq and field-effect mobility (μ_{eff}) of 962 $\text{cm}^2/(\text{V s})$ at room temperature. These electrical properties of the prepared graphene were competitive with those of previously reported transfer-free graphene films.

■ ASSOCIATED CONTENT

Supporting Information

The Supporting Information is available free of charge at <https://pubs.acs.org/doi/10.1021/acs.jpcc.0c05257>.

Details on the systematic investigation of CVD parameters; spectroscopic, nanoscopic, and microscopic characterization; Raman criteria for graphene monolayer; device fabrication; electrical measurement; and synthesis protocols (Tables S1 and S2; Figures S1–S14) (PDF)

■ AUTHOR INFORMATION

Corresponding Author

Chiao-Chen Chen – Department of Chemistry, National Cheng Kung University, Tainan City 701, Taiwan; orcid.org/0000-0002-7628-5706; Phone: +886 6 275-7575; Email: chiaochen@mail.ncku.edu.tw; Fax: +886 6 274-0552

Authors

Cheng-Yu Dai – Department of Chemistry, National Cheng Kung University, Tainan City 701, Taiwan

Wei-Chun Wang – Department of Chemistry, National Cheng Kung University, Tainan City 701, Taiwan

Chi-Ang Tseng – Department of Chemistry, National Taiwan University, Taipei 106, Taiwan

Fang-Chi Ding – Department of Chemistry, National Cheng Kung University, Tainan City 701, Taiwan

Yit-Tsong Chen – Department of Chemistry, National Taiwan University, Taipei 106, Taiwan; Institute of Atomic and Molecular Sciences Academia Sinica, Taipei 106, Taiwan; orcid.org/0000-0002-6204-8320

Complete contact information is available at: <https://pubs.acs.org/doi/10.1021/acs.jpcc.0c05257>

Notes

The authors declare no competing financial interest.

■ ACKNOWLEDGMENTS

The authors appreciate the assistance from Hui-Jung Shih (HR-SEM) and Tsai-Yun Liu (UHRFE-SEM) for the SEM characterizations and from Shih-Wen Tseng (HR-AEM) for the TEM operations. They are grateful to the Instrument Center and Center for Micro/Nano Science and Technology at National Cheng Kung University for providing the required technical support. The authors acknowledge the Ministry of Science and Technology of Taiwan for funding this study under grant nos. 105-2119-M-006-024-MY2 and 107-2113-M-006-010-MY3.

■ REFERENCES

- (1) Novoselov, K. S.; Geim, A. K.; Morozov, S. V.; Jiang, D.; Zhang, Y.; Dubonos, S. V.; Grigorieva, I. V.; Firsov, A. A. Electric Field Effect in Atomically Thin Carbon Films. *Science* **2004**, *306*, 666–669.
- (2) Jang, B. Z.; Huang, W. C. Nano-scaled Graphene Plates. US7,071,258B, 2006.
- (3) Castro Neto, A. H.; Guinea, F.; Peres, N. M. R.; Novoselov, K. S.; Geim, A. K. The Electronic Properties of Graphene. *Rev. Mod. Phys.* **2009**, *81*, 109–162.
- (4) Bonaccorso, F.; Sun, Z.; Hasan, T.; Ferrari, A. C. Graphene Photonics and Optoelectronics. *Nat. Photonics* **2010**, *4*, 611–622.
- (5) Pang, J.; Mendes, R. G.; Wrobel, P. S.; Wlodarski, M. D.; Ta, H. Q.; Zhao, L.; Giebeler, L.; Trzebicka, B.; Gemming, T.; Fu, L.; Liu, Z.; Eckert, J.; Bachmatiuk, A.; Rummeli, M. H. Self-Terminating Confinement Approach for Large-Area Uniform Monolayer Graphene Directly over Si/SiO_x by Chemical Vapor Deposition. *ACS Nano* **2017**, *11*, 1946–1956.
- (6) Reina, A.; Thiele, S.; Jia, X.; Bhaviripudi, S.; Dresselhaus, M. S.; Schaefer, J. A.; Kong, J. Growth of Large-Area Single- and Bi-Layer Graphene by Controlled Carbon Precipitation on Polycrystalline Ni Surfaces. *Nano Res.* **2009**, *2*, 509–516.
- (7) Li, X.; Zhu, Y.; Cai, W.; Borysiak, M.; Han, B.; Chen, D.; Piner, R. D.; Colombo, L.; Ruoff, R. S. Transfer of Large-Area Graphene Films for High-Performance Transparent Conductive Electrodes. *Nano Lett.* **2009**, *9*, 4359–4363.
- (8) Bae, S.; Kim, H.; Lee, Y.; Xu, X.; Park, J.-S.; Zheng, Y.; Balakrishnan, J.; Lei, T.; Kim, H. R.; Song, Y. I.; et al. Roll-to-Roll Production of 30-Inch Graphene Films for Transparent Electrodes. *Nat. Nanotechnol.* **2010**, *5*, 574–578.
- (9) Zhang, G.; Güell, A. G.; Kirkman, P. M.; Lazenby, R. A.; Miller, T. S.; Unwin, P. R. Versatile Polymer-Free Graphene Transfer Method and Applications. *ACS Appl. Mater. Interfaces* **2016**, *8*, 8008–8016.
- (10) Wang, D. Y.; Huang, I. S.; Ho, P. H.; Li, S. S.; Yeh, Y. C.; Wang, D. W.; Chen, W. L.; Lee, Y. Y.; Chang, Y. M.; Chen, C. C.; et al. Clean-Lifting Transfer of Large-Area Residual-Free Graphene Films. *Adv. Mater.* **2013**, *25*, 4521–4526.
- (11) Lin, W. H.; Chen, T. H.; Chang, J. K.; Taur, J. I.; Lo, Y. Y.; Lee, W. L.; Chang, C. S.; Su, W. B.; Wu, C. I. A Direct and Polymer-Free Method for Transferring Graphene Grown by Chemical Vapor Deposition to Any Substrate. *ACS Nano* **2014**, *8*, 1784–1791.
- (12) Wang, B.; Huang, M.; Tao, L.; Lee, S. H.; Jang, A. R.; Li, B. W.; Shin, H. S.; Akinwande, D.; Ruoff, R. S. Support-Free Transfer of Ultrasoft Graphene Films Facilitated by Self-Assembled Monolayers for Electronic Devices and Patterns. *ACS Nano* **2016**, *10*, 1404–1410.
- (13) Chen, M.; Stekovic, D.; Li, W.; Arkook, B.; Haddon, R. C.; Bekyarova, E. Sublimation-Assisted Graphene Transfer Technique Based on Small Polyaromatic Hydrocarbons. *Nanotechnology* **2017**, *28*, No. 255701.
- (14) Chen, J.; Wen, Y.; Guo, Y.; Wu, B.; Huang, L.; Xue, Y.; Geng, D.; Wang, D.; Yu, G.; Liu, Y. Oxygen-Aided Synthesis of Polycrystalline Graphene on Silicon Dioxide Substrates. *J. Am. Chem. Soc.* **2011**, *133*, 17548–17551.

- (15) Hwang, J.; Kim, M.; Campbell, D.; Alsalman, H. A.; Kwak, J. Y.; Shivaraman, S.; Woll, A. R.; Singh, A. K.; Hennig, R. G.; Gorantla, S.; Rummeli, M. H.; Spencer, M. G. Van der Waals Epitaxial Growth of Graphene on Sapphire by Chemical Vapor Deposition without a Metal Catalyst. *ACS Nano* **2013**, *7*, 385–395.
- (16) Yang, W.; Chen, G.; Shi, Z.; Liu, C.-C.; Zhang, L.; Xie, G.; Cheng, M.; Wang, D.; Yang, R.; Shi, D.; Watanabe, K.; Taniguchi, T.; Yao, Y.; Zhang, Y.; Zhang, G. Epitaxial Growth of Single-Domain Graphene on Hexagonal Boron Nitride. *Nat. Mater.* **2013**, *12*, 792–797.
- (17) Tang, S.; Wang, H.; Wang, H. S.; Sun, Q.; Zhang, X.; Cong, C.; Xie, H.; Liu, X.; Zhou, X.; Huang, F.; Chen, X.; Yu, T.; Ding, F.; Xie, X.; Jiang, M. Silane-Catalysed Fast Growth of Large Single-Crystalline Graphene on Hexagonal Boron Nitride. *Nat. Commun.* **2015**, *6*, No. 6499.
- (18) Sun, J.; Gao, T.; Song, X.; Zhao, Y.; Lin, Y.; Wang, H.; Ma, D.; Chen, Y.; Xiang, W.; Wang, J.; Zhang, Y.; Liu, Z. Direct Growth of High-Quality Graphene on High- κ Dielectric SrTiO₃ Substrates. *J. Am. Chem. Soc.* **2014**, *136*, 6574–6577.
- (19) Berger, C.; Song, Z.; Li, T.; Li, X.; Ogbazghi, A. Y.; Feng, R.; Dai, Z.; Marchenkov, A. N.; Conrad, E. H.; First, P. N.; de Heer, W. A. Ultrathin Epitaxial Graphite: 2D Electron Gas Properties and a Route toward Graphene-based Nanoelectronics. *J. Phys. Chem. B* **2004**, *108*, 19912–19916.
- (20) Berger, C.; Song, Z.; Li, X.; Wu, X.; Brown, N.; Naud, C.; Mayou, D.; Li, T.; Hass, J.; Marchenkov, A. N.; Conrad, E. H.; First, P. N.; de Heer, W. A. Electronic Confinement and Coherence in Patterned Epitaxial Graphene. *Science* **2006**, *312*, 1191–1196.
- (21) Shin, B. G.; Boo, D. H.; Song, B.; Jeon, S.; Kim, M.; Park, S.; An, E. S.; Kim, J. S.; Song, Y. J.; Lee, Y. H. Single-Crystalline Monolayer Graphene Wafer on Dielectric Substrate of SiON without Metal Catalysts. *ACS Nano* **2019**, *13*, 6662–6669.
- (22) Fanton, M. A.; Robinson, J. A.; Puls, C.; Liu, Y.; Hollander, M. J.; Weiland, B. E.; LaBella, M.; Trumbull, K.; Kasarda, R.; Howsare, C.; et al. Characterization of Graphene Films and Transistors Grown on Sapphire by Metal-Free Chemical Vapor Deposition. *ACS Nano* **2011**, *5*, 8062–8069.
- (23) Chen, J.; Guo, Y.; Jiang, L.; Xu, Z.; Huang, L.; Xue, Y.; Geng, D.; Wu, B.; Hu, W.; Yu, G.; Liu, Y. Near-Equilibrium Chemical Vapor Deposition of High-Quality Single-Crystal Graphene Directly on Various Dielectric Substrates. *Adv. Mater.* **2014**, *26*, 1348–1353.
- (24) Ismach, A.; Druzgalski, C.; Penwell, S.; Schwartzberg, A.; Zheng, M.; Javey, A.; Bokor, J.; Zhang, Y. Direct Chemical Vapor Deposition of Graphene on Dielectric Surfaces. *Nano Lett.* **2010**, *10*, 1542–1548.
- (25) Su, C.-Y.; Lu, A.-Y.; Wu, C.-Y.; Li, Y.-T.; Liu, K.-K.; Zhang, W.; Lin, S.-Y.; Juang, Z.-Y.; Zhong, Y.-L.; Chen, F.-R.; Li, L.-J. Direct Formation of Wafer Scale Graphene Thin Layers on Insulating Substrates by Chemical Vapor Deposition. *Nano Lett.* **2011**, *11*, 3612–3616.
- (26) Peng, Z.; Yan, Z.; Sun, Z.; Tour, J. M. Direct Growth of Bilayer Graphene on SiO₂ Substrates by Carbon Diffusion through Nickel. *ACS Nano* **2011**, *5*, 8241–8247.
- (27) Yan, Z.; Peng, Z.; Sun, Z.; Yao, J.; Zhu, Y.; Liu, Z.; Ajayan, P. M.; Tour, J. M. Growth of Bilayer Graphene on Insulating Substrates. *ACS Nano* **2011**, *5*, 8187–8192.
- (28) Kwak, J.; Chu, J. H.; Choi, J.-K.; Park, S.-D.; Go, H.; Kim, S. Y.; Park, K.; Kim, S.-D.; Kim, Y.-W.; Yoon, E.; Kodambaka, S.; Kwon, S.-Y. Near Room-Temperature Synthesis of Transfer-Free Graphene Films. *Nat. Commun.* **2012**, *3*, No. 645.
- (29) Lee, C. S.; Cojocar, C. S.; Moujahid, W.; Lebental, B.; Chaigneau, M.; Chatelet, M.; Le Normand, F.; Maurice, J. L. Synthesis of Conducting Transparent Few-Layer Graphene Directly on Glass at 450 Degrees C. *Nanotechnology* **2012**, *23*, No. 265603.
- (30) Kato, T.; Hatakeyama, R. Direct Growth of Doping-Density-Controlled Hexagonal Graphene on SiO₂ Substrate by Rapid-Heating Plasma CVD. *ACS Nano* **2012**, *6*, 8508–8515.
- (31) Sojoudi, H.; Graham, S. Transfer-Free Selective Area Synthesis of Graphene Using Solid-State Self-Segregation of Carbon in Cu/Ni Bilayers. *ECS J. Solid State Sci. Technol.* **2013**, *2*, M17–M21.
- (32) Xiong, W.; Zhou, Y. S.; Jiang, L. J.; Sarkar, A.; Mahjouri-Samani, M.; Xie, Z. Q.; Gao, Y.; Ianno, N. J.; Jiang, L.; Lu, Y. F. Single-Step Formation of Graphene on Dielectric Surfaces. *Adv. Mater.* **2013**, *25*, 630–634.
- (33) Pan, G.; Li, B.; Heath, M.; Horsell, D.; Wears, M. L.; Al Taan, L.; Awan, S. Transfer-Free Growth of Graphene on SiO₂ Insulator Substrate from Sputtered Carbon and Nickel Films. *Carbon* **2013**, *65*, 349–358.
- (34) McNerny, D. Q.; Viswanath, B.; Copic, D.; Laye, F. R.; Prohoda, C.; Brieland-Shoultz, A. C.; Polsen, E. S.; Dee, N. T.; Veerasamy, V. S.; Hart, A. J. Direct Fabrication of Graphene on SiO₂ Enabled by Thin Film Stress Engineering. *Sci. Rep.* **2014**, *4*, No. 5049.
- (35) Yang, G.; Kim, H.-Y.; Jang, S.; Kim, J. Transfer-Free Growth of Multilayer Graphene Using Self-Assembled Monolayers. *ACS Appl. Mater. Interfaces* **2016**, *8*, 27115–27121.
- (36) Wu, Z.; Guo, Y.; Guo, Y.; Huang, R.; Xu, S.; Song, J.; Lu, H.; Lin, Z.; Han, Y.; Li, H.; Han, T.; Lin, J.; Wu, Y.; Long, G.; Cai, Y.; Cheng, C.; Su, D.; Robertson, J.; Wang, N. A Fast Transfer-Free Synthesis of High-Quality Monolayer Graphene on Insulating Substrates by a Simple Rapid Thermal Treatment. *Nanoscale* **2016**, *8*, 2594–2600.
- (37) Vishwakarma, R.; Rosmi, M. S.; Takahashi, K.; Wakamatsu, Y.; Yaakob, Y.; Araby, M. I.; Kalita, G.; Kitazawa, M.; Tanemura, M. Transfer free graphene growth on SiO₂ substrate at 250 °C. *Sci. Rep.* **2017**, *7*, No. 43756.
- (38) Wang, Z.; Xue, Z.; Zhang, M.; Wang, Y.; Xie, X.; Chu, P. K.; Zhou, P.; Di, Z.; Wang, X. Germanium-Assisted Direct Growth of Graphene on Arbitrary Dielectric Substrates for Heating Devices. *Small* **2017**, *13*, No. 1700929.
- (39) Kang, D.; Kim, W.-J.; Lim, J. A.; Song, Y.-W. Direct Growth and Patterning of Multilayer Graphene onto a Targeted Substrate without an External Carbon Source. *ACS Appl. Mater. Interfaces* **2012**, *4*, 3663–3666.
- (40) Tamaoki, M.; Imaeda, H.; Kishimoto, S.; Mizutani, T. Transfer-Free Fabrication of Graphene Field Effect Transistor Arrays Using Solid-Phase Growth of Graphene on a SiO₂/Si Substrate. *Appl. Phys. Lett.* **2013**, *103*, No. 183114.
- (41) Zhuo, Q.-Q.; Wang, Q.; Zhang, Y.-P.; Zhang, D.; Li, Q.-L.; Gao, C.-H.; Sun, Y.-Q.; Ding, L.; Sun, Q.-J.; Wang, S.-D.; Zhong, J.; Sun, X.-H.; Lee, S.-T. Transfer-Free Synthesis of Doped and Patterned Graphene Films. *ACS Nano* **2015**, *9*, 594–601.
- (42) Ikuta, T.; Oe, T.; Ohno, Y.; Maehashi, K.; Inoue, K.; Matsumoto, K. Graphene Device Array Using Transfer-Free Patterning Growth on Insulator for an Electrolyte-Gated Sensor. *Thin Solid Films* **2016**, *612*, 87–90.
- (43) Fauzi, F. B.; Ismail, E.; Ani, M. H.; Syed Abu Bakar, S. N.; Mohamed, M. A.; Majlis, B. Y.; Md Din, M. F.; Azam Mohd Abid, M. A. A Critical Review of the Effects of Fluid Dynamics on Graphene Growth in Atmospheric Pressure Chemical Vapor Deposition. *J. Mater. Res.* **2018**, *33*, 1088–1108.
- (44) Chen, S.; Ji, H.; Chou, H.; Li, Q.; Li, H.; Suk, J. W.; Piner, R.; Liao, L.; Cai, W.; Ruoff, R. S. Millimeter-Size Single-Crystal Graphene by Suppressing Evaporative Loss of Cu During Low Pressure Chemical Vapor Deposition. *Adv. Mater.* **2013**, *25*, 2062–2065.
- (45) Chen, C.-C.; Kuo, C.-J.; Liao, C.-D.; Chang, C.-F.; Tseng, C.-A.; Liu, C.-R.; Chen, Y.-T. Growth of Large-Area Graphene Single Crystals in Confined Reaction Space with Diffusion-Driven Chemical Vapor Deposition. *Chem. Mater.* **2015**, *27*, 6249–6258.
- (46) An, S.; Lee, G.-H.; Jang, S. W.; Hwang, S.; Lim, S. H.; Han, S. A Facile Method for the Synthesis of Transfer-Free Graphene from Co-Deposited Nickel–Carbon Layers. *Carbon* **2016**, *109*, 154–162.
- (47) Weatherup, R. S.; Shahani, A. J.; Wang, Z.-J.; Mingard, K.; Pollard, A. J.; Willinger, M.-G.; Schloegl, R.; Voorhees, P. W.; Hofmann, S. In Situ Graphene Growth Dynamics on Polycrystalline Catalyst Foils. *Nano Lett.* **2016**, *16*, 6196–6206.

- (48) Liu, Y. P.; Liu, Z. W.; Lew, W. S.; Wang, Q. J. Temperature Dependence of the Electrical Transport Properties in Few-Layer Graphene Interconnects. *Nanoscale Res. Lett.* **2013**, *8*, No. 335.
- (49) Mattevi, C.; Kim, H.; Chhowalla, M. A Review of Chemical Vapor Deposition of Graphene on Copper. *J. Mater. Chem.* **2011**, *21*, 3324–3334.
- (50) Lin, H.-C.; Chen, Y.-Z.; Wang, Y.-C.; Chueh, Y.-L. The Essential Role of Cu Vapor for the Self-Limit Graphene via the Cu Catalytic CVD Method. *J. Phys. Chem. C* **2015**, *119*, 6835–6842.
- (51) Shin, Y. Y.; Lozada-Hidalgo, M.; Sambricio, J. L.; Grigorieva, I. V.; Geim, A. K.; Casiraghi, C. Raman Spectroscopy of Highly Pressurized Graphene Membranes. *Appl. Phys. Lett.* **2016**, *108*, No. 221907.
- (52) Wang, Y. y.; Ni, Z. h.; Yu, T.; Shen, Z. X.; Wang, H. m.; Wu, Y. h.; Chen, W.; Shen Wee, A. T. Raman Studies of Monolayer Graphene: The Substrate Effect. *J. Phys. Chem. C* **2008**, *112*, 10637–10640.
- (53) Cañado, L. G.; Jorio, A.; Ferreira, E. H. M.; Stavale, F.; Achete, C. A.; Capaz, R. B.; Moutinho, M. V. O.; Lombardo, A.; Kulmala, T. S.; Ferrari, A. C. Quantifying Defects in Graphene via Raman Spectroscopy at Different Excitation Energies. *Nano Lett.* **2011**, *11*, 3190–3196.
- (54) Yan, K.; Peng, H.; Zhou, Y.; Li, H.; Liu, Z. Formation of Bilayer Bernal Graphene: Layer-by-Layer Epitaxy via Chemical Vapor Deposition. *Nano Lett.* **2011**, *11*, 1106–1110.
- (55) Chen, Y.; Meng, L.; Zhao, W.; Liang, Z.; Wu, X.; Nan, H.; Wu, Z.; Huang, S.; Sun, L.; Wang, J.; Ni, Z. Raman Mapping Investigation of Chemical Vapor Deposition-Fabricated Twisted Bilayer Graphene with Irregular Grains. *Phys. Chem. Chem. Phys.* **2014**, *16*, 21682–21687.
- (56) Martins Ferreira, E. H.; Moutinho, M. V. O.; Stavale, F.; Lucchese, M. M.; Capaz, R. B.; Achete, C. A.; Jorio, A. Evolution of the Raman Spectra from Single-, Few-, and Many-Layer Graphene with Increasing Disorder. *Phys. Rev. B* **2010**, *82*, No. 125429.
- (57) Cañado, L. G.; Gomes da Silva, M.; Martins Ferreira, E. H.; Hof, F.; Kämpf, K.; Huang, K.; Pénicaud, A.; Alberto Achete, C.; Capaz, R. B.; Jorio, A. Disentangling Contributions of Point and Line Defects in the Raman Spectra of Graphene-Related Materials. *2D Mater.* **2017**, *4*, No. 025039.
- (58) Cañado, L. G.; Takai, K.; Enoki, T.; Endo, M.; Kim, Y. A.; Mizusaki, H.; Jorio, A.; Coelho, L. N.; Magalhães-Paniago, R.; Pimenta, M. A. General Equation for the Determination of the Crystallite Size L_a of Nanographite by Raman Spectroscopy. *Appl. Phys. Lett.* **2006**, *88*, No. 163106.
- (59) Jorio, A.; Cañado, L. G.; Malard, L. M. In *2D Materials: Properties and Devices*; Avouris, P.; Heinz, T. F.; Low, T., Eds.; Cambridge University Press: Cambridge, U.K., 2017; pp 79–83.
- (60) Rockett, A. *The Materials Science of Semiconductors*; Springer, 2007; pp 574–578.
- (61) Li, X.; Cai, W.; Colombo, L.; Ruoff, R. S. Evolution of Graphene Growth on Ni and Cu by Carbon Isotope Labeling. *Nano Lett.* **2009**, *9*, 4268–4272.
- (62) Liao, C.-D.; Lu, Y.-Y.; Tamalampudi, S. R.; Cheng, H.-C.; Chen, Y.-T. Chemical Vapor Deposition Synthesis and Raman Spectroscopic Characterization of Large-Area Graphene Sheets. *J. Phys. Chem. A* **2013**, *117*, 9454–9461.
- (63) Takesaki, Y.; Kawahara, K.; Hibino, H.; Okada, S.; Tsuji, M.; Ago, H. Highly Uniform Bilayer Graphene on Epitaxial Cu–Ni(111) Alloy. *Chem. Mater.* **2016**, *28*, 4583–4592.
- (64) Ding, D.; Solís-Fernández, P.; Hibino, H.; Ago, H. Spatially Controlled Nucleation of Single-Crystal Graphene on Cu Assisted by Stacked Ni. *ACS Nano* **2016**, *10*, 11196–11204.
- (65) Abidi, I. H.; Liu, Y.; Pan, J.; Tyagi, A.; Zhuang, M.; Zhang, Q.; Cagang, A. A.; Weng, L.-T.; Sheng, P.; Goddard, W. A., III; Luo, Z. Regulating Top-Surface Multilayer/Single-Crystal Graphene Growth by “Gettering” Carbon Diffusion at Backside of the Copper Foil. *Adv. Funct. Mater.* **2017**, *27*, No. 1700121.
- (66) Liu, X.; Fu, L.; Liu, N.; Gao, T.; Zhang, Y.; Liao, L.; Liu, Z. Segregation Growth of Graphene on Cu–Ni Alloy for Precise Layer Control. *J. Phys. Chem. C* **2011**, *115*, 11976–11982.
- (67) Wu, T.; Liu, Z.; Chen, G.; Dai, D.; Sun, H.; Dai, W.; Jiang, N.; Jiang, Y. H.; Lin, C.-T. A Study of the Growth-Time Effect on Graphene Layer Number Based on a Cu–Ni Bilayer Catalyst System. *RSC Adv.* **2016**, *6*, 23956–23960.
- (68) Batzill, M. The surface science of graphene: Metal interfaces, CVD synthesis, nanoribbons, chemical modifications, and defects. *Surf. Sci. Rep.* **2012**, *67*, 83–115.
- (69) Costa, S. D.; Righi, A.; Fantini, C.; Hao, Y.; Magnuson, C.; Colombo, L.; Ruoff, R. S.; Pimenta, M. A. Resonant Raman Spectroscopy of Graphene Grown on Copper Substrates. *Solid State Commun.* **2012**, *152*, 1317–1320.
- (70) Monville, M.; Rzhetskii, A.; Banerjee, S.; Strobl, K. In *Rapid Raman Quality Analysis of CVD Graphene Directly on Growth Substrates*, Nanotech Conference & Expo 2012, Proceedings of the Technical Proceedings of the 2012 NSTI Nanotechnology Conference and Expo, Santa Clara, CA, June 18–21, 2012;Laudon, M.; Romanowicz, B. F., Eds.; CRC Press: Santa Clara, CA, 2012.
- (71) Ferrari, A. C.; Basko, D. M. Raman Spectroscopy as a Versatile Tool for Studying the Properties of Graphene. *Nat. Nanotechnol.* **2013**, *8*, 235–246.
- (72) Hernandez, Y.; Nicolosi, V.; Lotya, M.; Blighe, F. M.; Sun, Z.; De, S.; McGovern, I. T.; Holland, B.; Byrne, M.; Gun'Ko, Y. K.; Boland, J. J.; Niraj, P.; Duesberg, G.; Krishnamurthy, S.; Goodhue, R.; Hutchison, J.; Scardaci, V.; Ferrari, A. C.; Coleman, J. N. High-Yield Production of Graphene by Liquid-Phase Exfoliation of Graphite. *Nat. Nanotechnol.* **2008**, *3*, 563–568.
- (73) Luo, B.; Chen, B.; Wang, A.; Geng, D.; Xu, J.; Wang, H.; Zhang, Z.; Peng, L.; Xu, Z.; Yu, G. Chemical Vapor Deposition of Bilayer Graphene with Layer-Resolved Growth through Dynamic Pressure Control. *J. Mater. Chem. C* **2016**, *4*, 7464–7471.
- (74) Pang, J.; Bachmatiuk, A.; Fu, L.; Mendes, R. G.; Libera, M.; Placha, D.; Martynková, G. S.; Trzebiecka, B.; Gemming, T.; Eckert, J.; Rummeli, M. H. Direct Synthesis of Graphene from Adsorbed Organic Solvent Molecules over Copper. *RSC Adv.* **2015**, *5*, 60884–60891.
- (75) Zhao, P.; Kumamoto, A.; Kim, S.; Chen, X.; Hou, B.; Chiashi, S.; Einarsson, E.; Ikuhara, Y.; Maruyama, S. Self-Limiting Chemical Vapor Deposition Growth of Monolayer Graphene from Ethanol. *J. Phys. Chem. C* **2013**, *117*, 10755–10763.
- (76) Song, H. J.; Son, M.; Park, C.; Lim, H.; Levendorf, M. P.; Tsen, A. W.; Park, J.; Choi, H. C. Large Scale Metal-Free Synthesis of Graphene on Sapphire and Transfer-Free Device Fabrication. *Nanoscale* **2012**, *4*, 3050–3054.
- (77) Goniszewski, S.; Adabi, M.; Shaforost, O.; Hanham, S. M.; Hao, L.; Klein, N. Correlation of p-doping in CVD Graphene with Substrate Surface Charges. *Sci. Rep.* **2016**, *6*, No. 22858.
- (78) Moser, J.; Verdager, A.; Jiménez, D.; Barreiro, A.; Bachtold, A. The Environment of Graphene Probed by Electrostatic Force Microscopy. *Appl. Phys. Lett.* **2008**, *92*, No. 123507.
- (79) Lin, Y. C.; Chiu, P. W. In *Graphene: Properties, Preparation, Characterisation and Devices*; Skákalová, V.; Kaiser, A. B., Eds.; Elsevier: Massachusetts, 2014; pp 265–291.

Supporting Information

A Spatial Confinement Approach Using Ni to modulate Local Carbon Supply for the Growth of Uniform Transfer-Free Graphene Monolayers

Cheng-Yu Dai,[†] Wei-Chun Wang,[†] Chi-Ang Tseng,[‡] Fang-Chi Ding,[†] Yit-Tsong Chen^{‡,§} and Chiao-Chen Chen^{†,*}

[†]Department of Chemistry
National Cheng Kung University
No.1, University Road
Tainan City 701, Taiwan

[‡]Department of Chemistry
National Taiwan University
No. 1, Sec. 4, Roosevelt Road
Taipei 106, Taiwan

[§]Institute of Atomic and Molecular Sciences
Academia Sinica
P.O. Box 23-166
Taipei 106, Taiwan

* Author to whom correspondence should be addressed.

E-mail: chiaochen@mail.ncku.edu.tw; Phone: +886 6 275-7575 ext.65354; Fax: +886 6 274-0552

Section 1: Spectroscopic, nanoscopic, and microscopic characterization

After the chemical vapor deposition (CVD) process, the transfer-free graphene grown at the metal–SiO₂ interface was exposed by chemical etching of the deposited metal film with 0.1 M ammonium persulfate (Alfa Aesar, 98.0%). The exposed transfer-free graphene on the SiO₂/Si substrate was then characterized by micro-Raman microscopy (HORIBA Jobin Yvon/Labram HR) using a 50-mW solid-state laser, which was focused by a 100× objective to have a beam size of approximately 1 μm² and exhibited an excitation wavelength of 532 nm. For all the Raman measurements, Raman shifts were recorded from 1200 to 3500 cm⁻¹ and the characteristic peak of Si at 520.7 cm⁻¹ was utilized as an internal standard to calibrate the spectral position. In addition to point measurement, Raman mapping was also conducted by imaging a matrix of 64 × 64 pixels over an area of 75 × 75 μm² (~1.17 μm/pixel), with an accumulation time of 1.5 sec at each spot. The surface morphology of the deposited metal films and synthesized transfer-free graphene were characterized using an optical microscope (Olympus, BX51M) equipped with a charge-coupled device camera (Jenoptik C14 plus) as well as a field-emission scanning electron microscope (HITACHI SU8000 and Zeiss AURIGA Compact FIB-SEM) and atomic force microscope (Bruker, Dimension Icon) for microscopic and nanoscopic examination, respectively. High-resolution transmission electron microscopy (TEM; JEOL JEM-2100F) was performed at 200 kV to examine the layer numbers and crystallinity of the produced graphene.

Section 2: Effects of CVD parameters on graphene synthesis

To successfully prepare homogenous large-area transfer-free graphene, crucial CVD parameters were systematically investigated. For determining the appropriate reaction temperature, graphene samples prepared at different temperatures were examined. A graphite-like material with high nucleation density and thus ultra-small grains (*i.e.*, nanocrystalline graphite) was obtained in a low-temperature regime. The Raman measurements of samples prepared at different temperatures (Figures 3b and S1b and Table S2, P2–P6) indicated that nanocrystalline graphite was formed at ≤ 900 °C. This result was confirmed by the following spectral evidence: (1) blue shift of the G band from 1581 (the characteristic of monolayer graphene) to approximately 1600 cm^{-1} , (2) a negligible 2D band, and (3) high I_D/I_G ratios.^{S1-3} The sample obtained at 1000 °C exhibited a similar average I_{2D}/I_G ratio as that obtained at 1050 °C, which implied these graphene samples had comparable film thickness. However, the sublimation and dewetting of the deposited Cu film were more serious at 1050 °C, which led to the deteriorated integrity of the Cu film. The deteriorated integrity of the Cu film resulted in degraded uniformity of the produced graphene, as indicated by a greater variation in the I_{2D}/I_G ratios for the sample obtained at 1050 °C than that obtained at 1000 °C (Figure 3b). Therefore, a reaction temperature of 1000 °C was selected for the remaining experiments.

It has been reported that crystalline structure of the metal film influences the quality of the transfer-free graphene synthesized at the metal–dielectric interface.^{S4} In addition, the grain size and thus the density of the metal grain boundaries are considerably affected by the annealing process, which is a heat treatment procedure commonly applied to alter the microstructure of metals. In this study, the annealing duration did exert a distinct influence on the copper grain size and the quality

of the produced graphene. The Cu film prepared through sputtering deposition was composed of nanocrystallites (Figure S2a). After 40 min of temperature ramping at a speed of 25 °C/min from room temperature to 1000 °C, the deposited Cu film underwent recrystallization, which considerably increased its grain diameter from <200 nm (Figure S2a) to 2–20 μm (Figure S2b). By maintaining the temperature at 1000 °C, the grain diameter further expanded to approximately 10–40 μm with an annealing duration of 30 min, which led to a considerable decrease in the total length of the grain boundaries (Figure S2e). A reduction in the grain boundary length is believed to suppress the nucleation density of the produced transfer-free graphene by slowing down the supersaturation of interfacial carbon species, which reach the Cu–SiO₂ interface mainly through grain boundary diffusion rather than bulk diffusion due to the low carbon solubility of Cu.

In addition, interfacial carbon species are preferentially nuclearized along the Cu grain boundaries due to their relatively high surface energy.^{S5} This assumption was verified by examining the traces of the metal grain boundaries in the produced transfer-free graphene samples,^{S6, 7} particularly on the exposed SiO₂ surface that was not covered by a confluent graphene films (Figure S3, white arrows). These traces are considered to be amorphous carbon (a-C) or diamond-like carbon accumulated by carbon species, which diffuse through the Cu film to be deposited along the metal grain boundaries before recrystallization to form graphene films.^{S6} For the Cu films subjected only to a temperature ramping process without an extended annealing time (*i.e.*, annealing for 0 min), the resultant sample was nanocrystalline graphite with a negligible 2D band (black line in Figure S1c). By contrast, the quality of the transfer-free graphene significantly improved in terms of

the reduced defect density (I_D/I_G decreased from 0.62 to 0.37) and the decreased layer number (I_{2D}/I_G increased from 0.10 to 0.58) with the extension of the annealing time (Figures 3c and S1c; Table S2, P7–P10). Correlating the morphology observations of the Cu film (Figure S2) with the Raman measurements of graphene (Figures 3c and S1c) indicates that without sufficient annealing time, the Cu film tends to consist of small grains with dense grain boundaries. Consequently, excessive carbon accumulates at the Cu–SiO₂ interface, which leads to the formation of nanocrystalline graphite rather than thin-layer graphene. Therefore, an annealing time of 30 min was applied in addition to 40-min temperature ramping for graphene synthesis in this study.

To determine an appropriate duration for graphene growth, graphene samples prepared with various growth times were investigated (Table S2, P10–P12). The Raman measurements (Figures 3d and S1d) indicated that the I_{2D}/I_G ratio decreased monotonically with an increase in the growth time within the range of 5–30 min. This result suggested that the layer number of the produced graphene increased with the growth duration, which is proportional to the amount of carbon species available for thin-film deposition. In addition, the I_D/I_G ratio decreased to a local minimum with considerably reduced fluctuation when the growth time was >15 min, which implied that a confluent graphene film began to form at around 15 min of growth. This assumption was verified through atomic force microscopy (AFM) characterization. For the sample subjected to 2 min of growth, no detectable thin-film structure but subtle traces of Cu grain boundaries were observed on the surface of the SiO₂/Si substrate after the removal of the Cu film (Figure S4a). Thin-film structures were observed for the samples subjected to 5-min growth (Figure S4b), and the coverage

of the produced graphene film reached approximately 87% for 10-min growth (Figure S4c). At the end of 15-min growth, a confluent graphene film was obtained without noticeable pin holes or cracks (Figure S4d). The AFM results for the evolution of the graphene film are consistent with the Raman measurements. This phenomenon confirms that although 5-min growth is beneficial for the formation of graphene having few layers and a relatively high I_{2D}/I_G ratio, the produced graphene film is not continuous and thus displays a high number of structural defects and low uniformity, as indicated by the high I_D/I_G ratio with a large fluctuation. Consequently, a growth time of 15 min was selected for the synthesis of large-area transfer-free graphene with high uniformity.

The composition of reactant flows also influences the final quality of the produced graphene. In this study, the reactants utilized included Ar as the carrier gas, H_2 as the co-catalyst, and CH_4 as the carbon source. Argon is commonly used as an inert carrier gas to dilute the concentrations of active reactants (H_2 and CH_4 in this study), which are preferentially kept low to limit the carbon deposition rate for preventing the excessive formation of graphene nuclei and layers.^{S8} As displayed in Figures 3e and S1e (Table S2, P10 and P13–P16), when the flow rates of H_2 and CH_4 were maintained at 15 and 1 sccm, respectively, the quality of the produced graphene could be improved by increasing the Ar supply. The improvement in the quality was verified by the enhanced I_{2D}/I_G ratios (*i.e.*, reduced layer number) and reduced I_D/I_G ratios (*i.e.*, decrease in structural defects). Both these ratios stabilized when an Ar flow of at least 100 sccm was utilized (Figure 3e). Therefore, an Ar flow of 200 sccm was applied for saving reagent and achieving suitable reproducibility in product quality. Furthermore, when the flow rates of Ar and H_2 were

maintained at 200 and 15 sccm, respectively, the I_{2D}/I_G ratio of the produced graphene decreased monotonically with an increase in the methane supply as long as the flow rate of CH_4 was >1 sccm (Figures 3f and S1f; Table S2, P10 and P17–P19). The trend of the I_{2D}/I_G ratio changed at a CH_4 flow rate of 0.5 sccm possibly because of the insufficient carbon supply for graphene growth and the relatively unstable control of the mass flow meter at low flow rate. Consequently, graphene produced with a CH_4 flow rate of 0.5 sccm exhibited a relatively low average I_{2D}/I_G value with a large fluctuation, which implied that the produced film had degraded uniformity and limited two-dimensional crystallinity. As a co-catalyst, hydrogen has a complicated influence on the growth mechanism of graphene. It improves the catalytic capability of Cu by eliminating contaminants and oxides on Cu^{S9} and affects graphene growth by altering the kinetics of methane dissociation and hydrogen etching.^{S10, 11} Therefore, appropriate relative amounts of H_2 and CH_4 should be used to balance efficient methane dissociation with limited hydrogen etching. Under a constant CH_4 flow rate of 1 sccm, low-defect graphene with the smallest thickness (*i.e.*, the highest I_{2D}/I_G ratio) was obtained when using a H_2 flow rate of 15 sccm (Figures 3g and S1g; Table S2, P10 and P20–P26).

Section 3: Raman criteria utilized to determine graphene monolayer

Raman criteria utilized in this study for monolayer graphene are assigned to be >1.4 for the I_{2D}/I_G ratio and $24\text{--}45\text{ cm}^{-1}$ for the FWHM of 2D peak (Γ_{2D}) based on several reported studies.^{S12-15} Although not strictly following the classical standards (*i.e.*, >2 for the I_{2D}/I_G ratio and $24\text{--}30\text{ cm}^{-1}$ for Γ_{2D}) defined for exfoliated graphene monolayer, the Raman criteria utilized here are generally accepted for graphene films prepared with CVD method. Deviations in the Raman characteristics of

the synthesized graphene from those of the exfoliated graphene have been attributed to several factors, including the structural defects^{S16, 17} and mechanical strains^{S18} on the synthesized graphene films as well as the substrate effects.^{S19} In our case, structural defects on the produced graphene could be the main reason for both the reduced I_{2D}/I_G ratio and the 2D band broadening. As discussed in the main text, band broadening was also observed in G band ($>15 \text{ cm}^{-1}$) from our products, implying that the graphene samples produced here possessed a relatively high amount of structural defects. From the reported relationship between the FWHM of G peak and the average distance between point defects (L_D) (the dashed line in Figure S5c),^{S16} the L_D of the graphene synthesized here was determined to be about 4 nm corresponding to a point defect density (σ) of $\sim 0.02 \text{ nm}^{-2}$ (the blue sphere in Figure 4d). Because of this small L_D , the 2D band width (Γ_{2D}) of the graphene monolayer prepared in this study displayed an averaged value of $39.3 \pm 2.78 \text{ cm}^{-1}$, which is in good agreement with the reported Γ_{2D} of about 40 cm^{-1} for monolayer graphene with $L_D = 4 \text{ nm}$ (Figure S5a). In addition, from the reported relationship between L_D and the normalized intensity of 2D (also noted as G' band) and G bands (Figure S5b), the ratio of I_{2D}/I_G was estimated to be ~ 1 for monolayer graphene with $L_D = 4 \text{ nm}$, consistent with the Raman criterion of the I_{2D}/I_G ratio > 1.4 for the graphene monolayer synthesized in this study.

Section 4: Device fabrication and electrical measurement

Graphene field-effect-transistors (GFETs) were fabricated from the transfer-free graphene patterns synthesized in this study. A TEM copper grid was utilized as a shadow mask for the thermal-evaporation deposition of source and drain electrodes (10-nm Cr/50-nm Au) on the

graphene patterns. The fabricated GFETs were annealed at 250 °C under an inert atmosphere (100 sccm of Ar) for 2 h to improve the metal–graphene contact. Electrical measurements of the annealed GFETs were performed using a probe station (Lakeshore, TTPX) equipped with a source meter (Keithley, 2636A) under vacuum ($\sim 2 \times 10^{-3}$ Torr) at room temperature. For all the measurements, a back-gate voltage (V_g) was applied to the Si substrate with a 300-nm-thick SiO₂ layer. Using the transfer curve (I_{sd} – V_g) recorded at a source–drain voltage (V_{sd}) of 0.1 V, the device resistance (R_{tot}) determined from ohm’s law ($R_{tot} = V_{sd}/I_{sd}$) can be expressed as a combination of the metal–graphene contact resistance ($R_{contact}$) and the graphene channel resistance ($R_{channel}$), as described in eq S1.^{S20, 21}

$$\begin{aligned}
 R_{tot} &= \frac{V_{sd}}{I_{sd}} = R_{contact} + R_{channel} = R_{contact} + \frac{L}{W} \cdot \rho \\
 &= R_{contact} + \frac{L}{W} \cdot \frac{1}{\mu_{EF} \sqrt{e^2 n_0^2 + [C_g (V_g - V_{Dirac})]^2}} \quad (S1)
 \end{aligned}$$

In eq S1, L refers to the channel length between the source and drain electrodes; W is the channel width; and ρ denotes the channel resistivity, which is a function of the field-effect mobility (μ_{EF}), elementary charge (e), residual carrier density (n_0), capacitance of the 300-nm-thick SiO₂ layer ($C_g = 11.5$ nF/cm²), and difference between the gate voltage (V_g) and the potential shift at the Dirac point (V_{Dirac}).

Table S1. Comparison of Representative Protocols^{a)} for the Synthesis of Large-Area Transfer-Free Graphene Using the Metal-Catalyzed CVD Process

Ref.	Synthesis parameters					Figure of merit for the quality of transfer-free graphene					
	Reactor type	Substrate for synthesis	Carbon source	Growth temp. (°C)	Synthesis duration ^{b)} (min)	Size of the continuous film (cm ²)	Average I_{2D}/I_G	Average I_D/I_G	Layer number [‡]	Sheet resistance (Ω/sq)	mobility (cm ² /Vs)
25	Free space ^{c)}	Cu/SiO ₂ /Si	CH ₄	900	30	5.1	1.6	0.1	2 layers	2000	672
26	In Cu enclosure	PMMA/Ni/SiO ₂ /Si	PMMA ^{d)}	1000	10	N.A.	1.11	< 0.1	20% monolayer 70% bilayer 10% few-layer	2000	N.A.
27	In Cu enclosure	Ni/PPMS/SiO ₂ /Si	PPMS ^{d)}	1000	7-20	1.0	1.0	0.1	2 layers	2000	160 ± 41
28	Free space	Graphite/Ni/SiO ₂ /Si	Graphite	160	5	1-2	0.83 ± 0.13	0.24 ± 0.08	1-few layers	977	667
29	Free space	Ni/glass	CH ₄	450	12	N.A.	0.28	1.18	1-30 layers	500	N.A.
30	Free space	Ni/SiO ₂ /Si	CH ₄	950	3	1.0	1.8	< 0.1	1-2 layers	N.A.	362
31	Free space	Cu/Ni/SiO ₂ /Si	Co-deposited carbon in metal	1000	30	50	1.48 ± 0.16	0.18 ± 0.08	1-2 layers	N.A.	N.A.
32	Free space	Ni/a-C/SiO ₂ /Si	amorphous C	1100	2	81	1.42 ± 0.05	0.16 ± 0.08	92% monolayer 7% bilayer 1% few-layer	50	N.A.
33	Free space	Ni/SiC/SiO ₂ /Si SiC/Ni/SiO ₂ /Si	amorphous C or SiC	1000	2	N.A.	N.A.	<0.1	40% monolayer	N.A.	N.A.
34	Free space	Ni/SiO ₂ /Si	C ₂ H ₂	875	7	1.0	0.57	0.13	2-few layers	N.A.	N.A.
35	Free space	Cu/PhSi(OMe) ₃ /SiO ₂ /Si	PhSi(OMe) ₃ ^{d)}	1000	30	1.0	0.48	0.42	7 layers	3500	N.A.
36	Free space	PMMA/Cu/SiO ₂ /Si	PMMA ^{d)}	1000	4-8	0.01 (= 1 mm ²) ^{e)}	1.8	0.05	monolayer	N.A.	2800
37	Free space	Sn/a-C/SiO ₂ /Si	amorphous C	250	N.A.	N.A.	0.44	0.14	15-20 layers	N.A.	N.A.
38	Free space	Ge/SiO ₂ /Si	CH ₄	920	300	1.0	1.42 ± 0.18	0.71 ± 0.20	monolayer	N.A.	730
This work	Confined space	Cu/SiO ₂ /Si	CH ₄	1000	45	1.0	1.96 ± 0.31	0.21 ± 0.11	91% monolayer 9% bilayer	334	962

^{a)} These representative works are the top 14 of ~50 studies reported since 2009 for preparing transfer-free graphene using deposited metal film on Si substrates, which are selected by evaluating the produced graphene quality in terms of film continuity, layer numbers, uniformity and the defective level.

^{b)} The synthesis duration includes the annealing and growth periods to obtain a continuous graphene film.

^{c)} “Free space” indicates that the substrate was located in a conventional CVD furnace without special design for the modulation of the fluid dynamics.

- d) PMMA: poly(methyl methacrylate), PPMS: poly(2-phenylpropyl)methylsiloxane, PhSi(OMe)₃: trimethoxyphenylsilane.
- e) Transfer-free graphene films with less competitive quality than that achieved in this study are shaded in gray.

Table S2. Synthesis Protocols Utilized in This Study

Protocol	Temp. (°C)	Annealing step			Growth step					Reactor type	Catalyst composition	
		Pressure (Torr)	Ar (sccm)	H ₂ (sccm)	Time (min)	Pressure (Torr)	Ar (sccm)	H ₂ (sccm)	CH ₄ (sccm)	Time (min)		Confined space (mm)
P0	1000	floating at ~1.10	200	10	30	floating at ~1.12	200	15	1	15	Free space	Cu 400 nm
P1	1000	floating at ~1.10	200	10	30	floating at ~1.12	200	15	1	15	0.65	Cu 400 nm
P2	700	90	200	10	5	90	200	15	1	30	0.65	Cu 400 nm
P3	800	90	200	10	5	90	200	15	1	30	0.65	Cu 400 nm
P4	900	90	200	10	5	90	200	15	1	30	0.65	Cu 400 nm
P5	1000	90	200	10	5	90	200	15	1	30	0.65	Cu 400 nm
P6	1050	90	200	10	5	90	200	15	1	30	0.65	Cu 400 nm
P7	1000	90	200	10	0	90	200	15	1	15	0.65	Cu 400 nm
P8	1000	90	200	10	5	90	200	15	1	15	0.65	Cu 400 nm
P9	1000	90	200	10	20	90	200	15	1	15	0.65	Cu 400 nm
P10	1000	90	200	10	30	90	200	15	1	15	0.65	Cu 400 nm
P11	1000	90	200	10	30	90	200	15	1	5	0.65	Cu 400 nm
P12	1000	90	200	10	30	90	200	15	1	30	0.65	Cu 400 nm
P13	1000	90	200	10	30	90	0	15	1	15	0.65	Cu 400 nm
P14	1000	90	200	10	30	90	25	15	1	15	0.65	Cu 400 nm
P15	1000	90	200	10	30	90	50	15	1	15	0.65	Cu 400 nm
P16	1000	90	200	10	30	90	100	15	1	15	0.65	Cu 400 nm
P17	1000	90	200	10	30	90	200	15	0.5	15	0.65	Cu 400 nm
P18	1000	90	200	10	30	90	200	15	3	15	0.65	Cu 400 nm
P19	1000	90	200	10	30	90	200	15	5	15	0.65	Cu 400 nm
P20	1000	90	200	10	30	90	200	10	1	15	0.65	Cu 400 nm
P21	1000	90	200	10	30	90	200	12.5	1	15	0.65	Cu 400 nm
P22	1000	90	200	10	30	90	200	17.5	1	15	0.65	Cu 400 nm
P23	1000	90	200	10	30	90	200	20	1	15	0.65	Cu 400 nm
P24	1000	90	200	10	30	90	200	25	1	15	0.65	Cu 400 nm
P25	1000	90	200	10	30	90	200	30	1	15	0.65	Cu 400 nm
P26	1000	90	200	10	30	90	200	40	1	15	0.65	Cu 400 nm
P27	1000	90	200	10	30	90	200	15	1	15	0.65	Cu 500 nm
P28	1000	90	200	10	30	90	200	15	1	15	0.65	Cu 640 nm
P29	1000	90	200	10	30	90	200	15	1	15	0.65	Cu 700 nm
P30	1000	90	200	10	30	90	200	15	1	15	0.65	Cu 800 nm

Table S2. Synthesis Protocols utilized in This Study (Continued)

Protocol	Temp. (°C)	Annealing step			Growth step					Reactor type Confined space (mm)	Catalyst composition	
		Pressure (Torr)	Ar (sccm)	H ₂ (sccm)	Time (min)	Pressure (Torr)	Ar (sccm)	H ₂ (sccm)	CH ₄ (sccm)			Time (min)
P31	1000	90	200	10	30	90	200	15	1	15	0.65	Cu1000 nm
P32	1000	90	200	10	30	90	200	15	1	15	0.55	Cu 700 nm
P33	1000	90	200	10	30	90	200	15	1	15	0.75	Cu 700 nm
P34	1000	90	200	10	30	90	200	15	1	15	1.20	Cu 700 nm
P35	1000	90	200	10	30	90	200	15	1	15	0.55	Cu 665 nm/Ni 35 nm
P36	1000	90	200	10	30	90	200	15	1	15	0.55	Cu 630 nm/Ni 70 nm
P37	1000	90	200	10	30	90	200	15	1	15	0.55 (Ni Cover)	Cu 700 nm
P38	1000	90	200	10	30	90	200	15	1	15	0.55 (Ni Cover)	Patterned Cu 700 nm

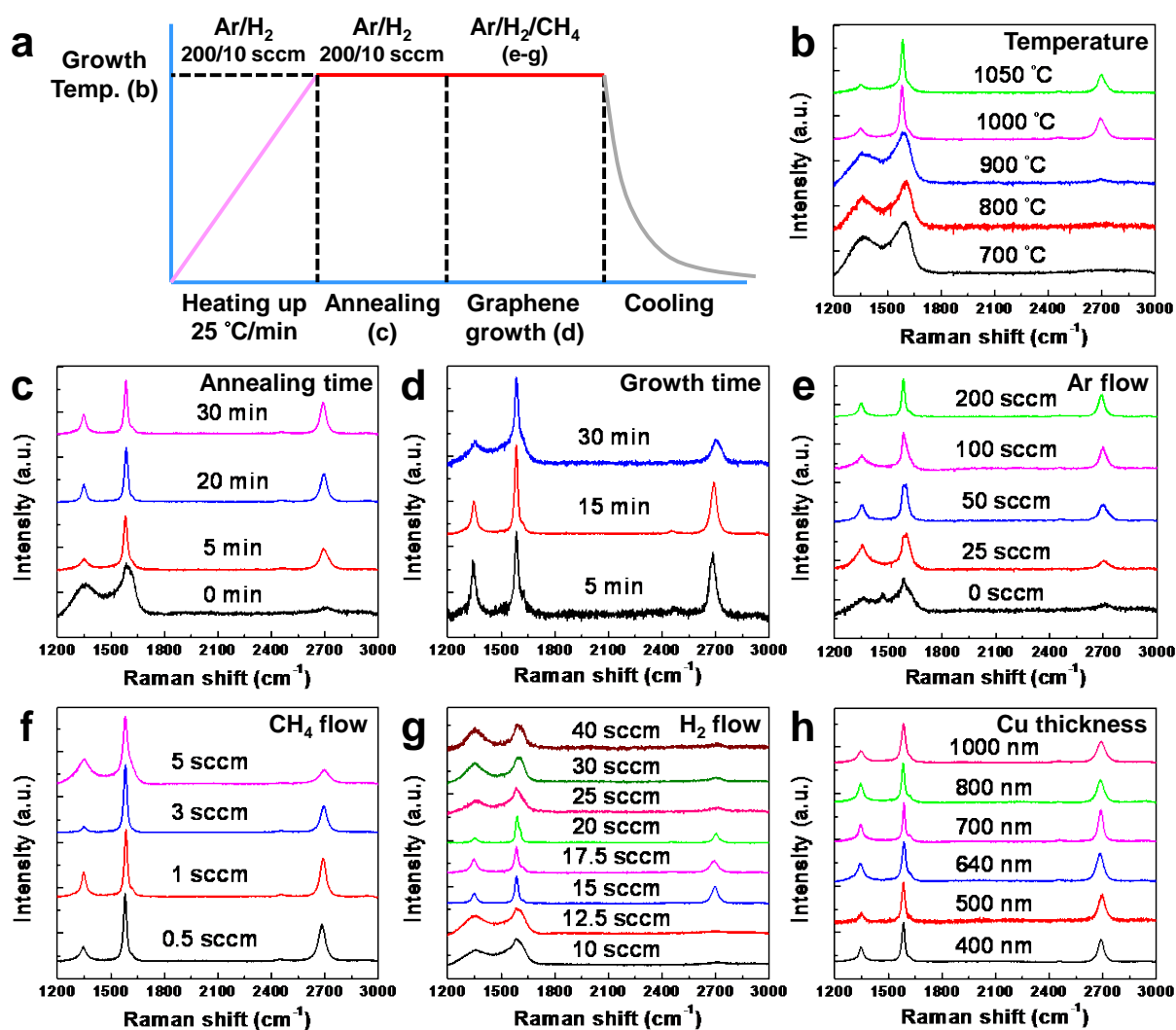


Figure S1. (a) Workflow diagram for the CVD synthesis of transfer-free graphene in this study. The effects of CVD parameters, namely the (b) growth temperature, (c) annealing time, (d) growth time, (e) Ar flow rate, (f) CH₄ flow rate, (g) H₂ flow rate, and (h) Cu film thickness, on the quality of produced graphene were examined using Raman spectra.

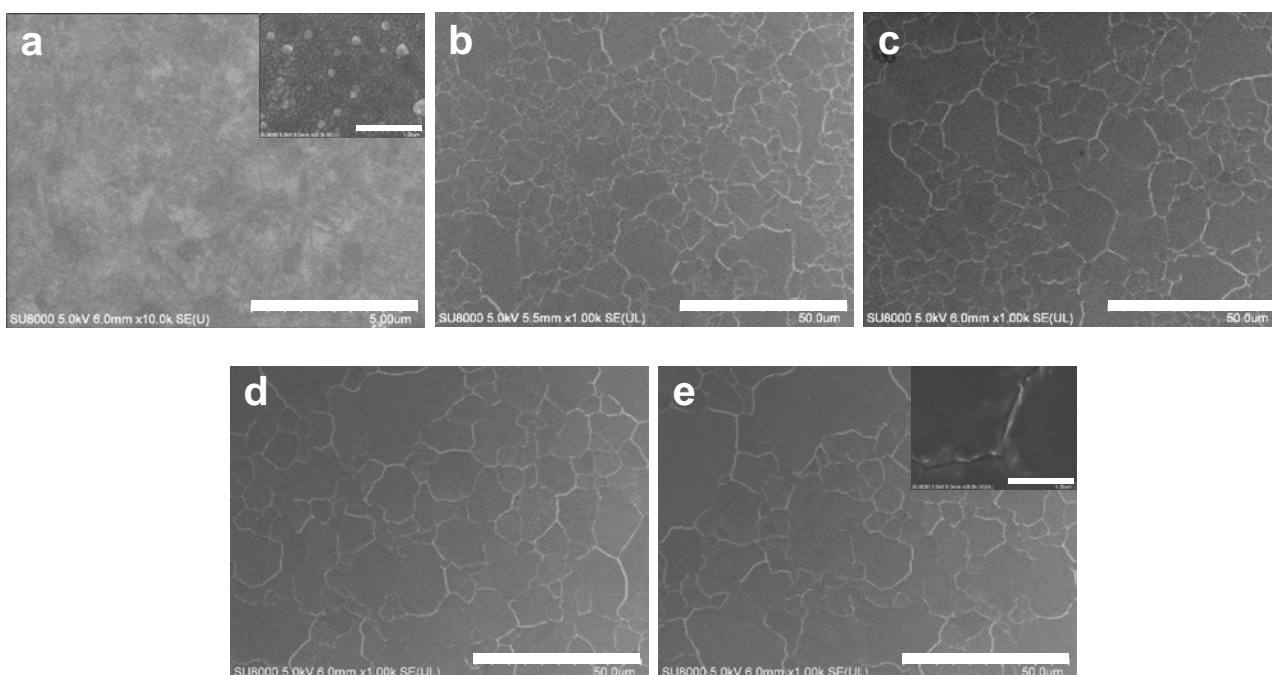


Figure S2. Scanning electron microscopy (SEM) images of the morphology of (a) an as-deposited Cu film, (b) the deposited Cu film subjected to 40-min heating from room temperature to 1000 °C, (c) the Cu film annealed at 1000 °C for 5 min after the heating-up process, (d) the Cu film annealed at 1000 °C for 20 min after the heating-up process, and (e) the Cu film annealed at 1000 °C for 30 min after the heating-up process. Scale bar of (a–e): 5 μm . The insets of (a) and (e) are zoomed-in images that indicate that an extended annealing time considerably increases the Cu grain size and reduces the grain boundary length per unit area. Scale bar for the insets of (a) and (e): 1 μm .

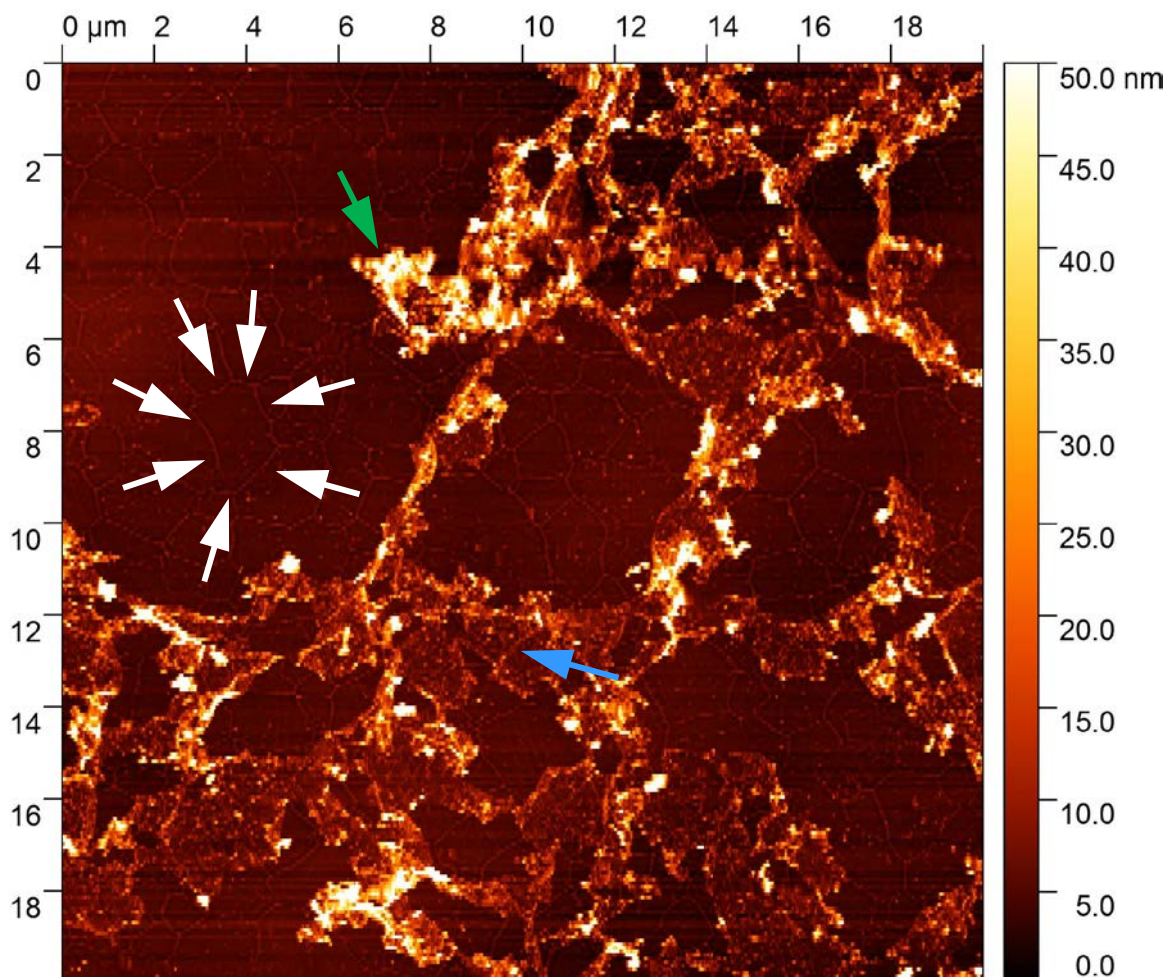


Figure S3. AFM image of a transfer-free graphene sample on a SiO₂/Si substrate prepared with an insufficient growth time (5 min). Since the growth time was too short to develop a confluent graphene film, a significant portion of the substrate surface was exposed on which the traces of the Cu grain boundaries were clearly observed (white arrows). The traces of the Cu grain boundaries were also observed on the graphene film (blue arrow); however, the boundaries were less clear due to possible interference from the wrinkles and ripples of the graphene film. In addition, because the graphene film was not confluent, it was difficult to prevent detachment and folding (green arrow) at the edge of the graphene thin film during the process of Cu removal *via* wet-chemical etching.

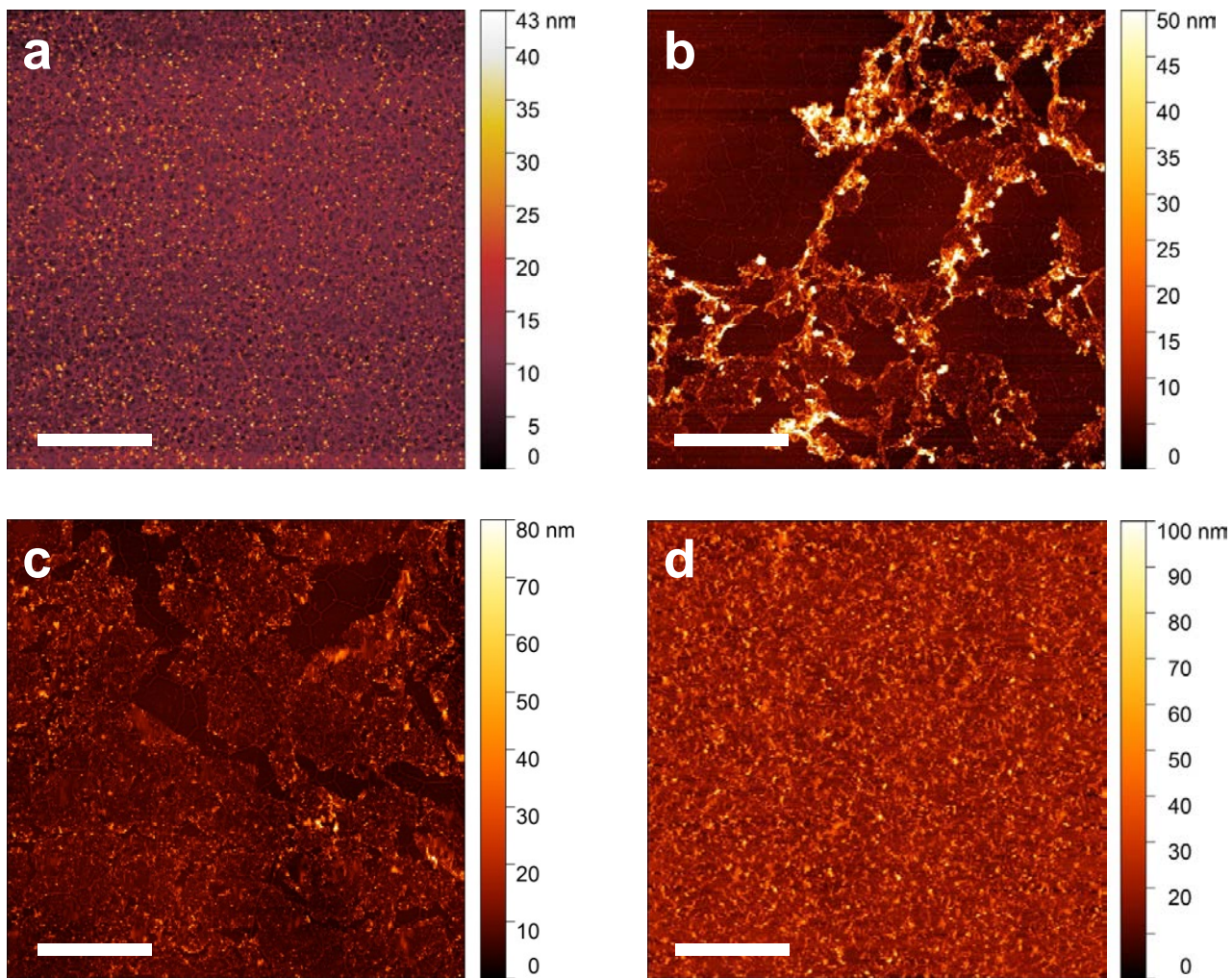


Figure S4. AFM images of the transfer-free graphene samples obtained with a growth time of (a) 2, (b) 5, (c) 10, and (d) 15 min. Scale bar: 5 μm .

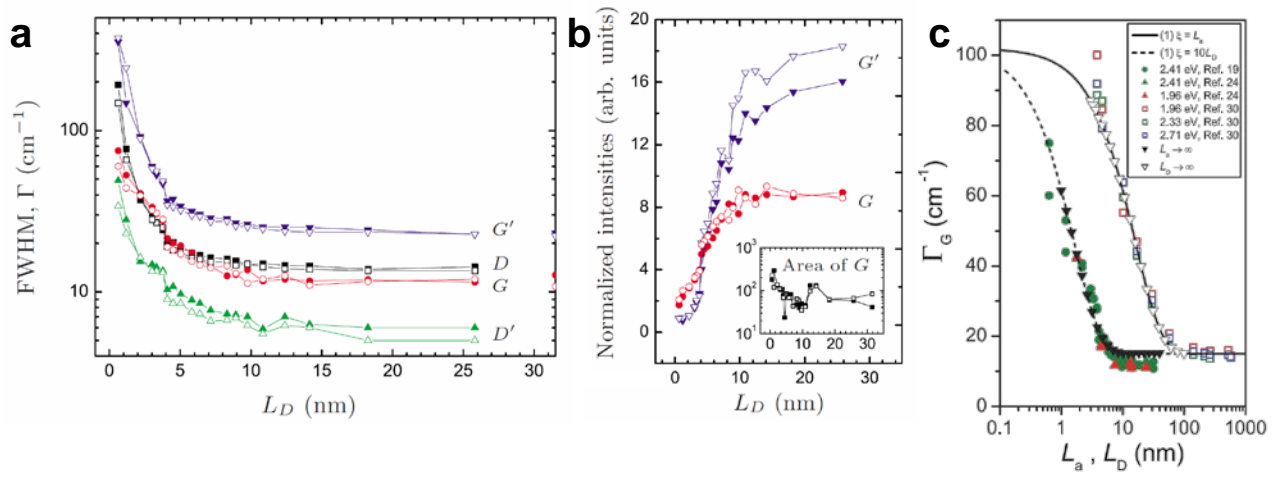


Figure S5. (a) The full width at half maximum (FWHM) of the G' ($2D$), D , G and D' bands as a function of L_D (the distance between point defects) for monolayer graphene. (b) The intensities of G' ($2D$) and G bands were normalized by the integrated area of G band and were plotted as a function of L_D for monolayer graphene. Reprinted with permission from ref. S17. Copyright 2010 American Physical Society. (c) The full width at half maximum (FWHM) of the G band (Γ_G) as a function of L_D and L_a (the distance between line defects) for graphene-related materials. Reprinted with permission from ref. S16. Copyright 2017 IOP Publishing Limited.

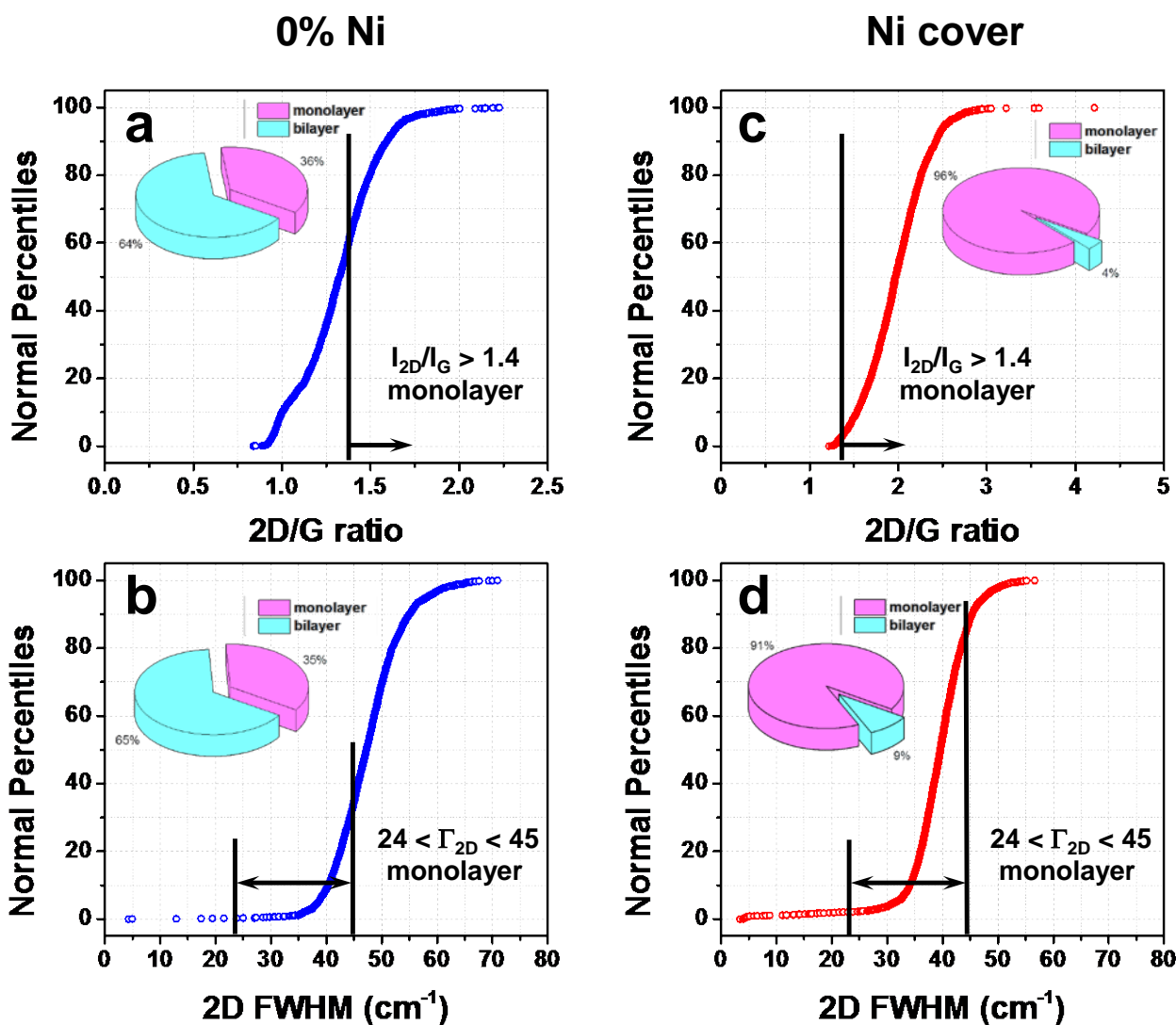


Figure S6. For the transfer-free graphene prepared using pure Cu films within a quartz slit reactor (denoted as 0% Ni), the cumulative count plots of the (a) I_{2D}/I_G ratios and (b) FWHM of the 2D band determined from Raman measurements indicated that the graphene was composed of 35% monolayers and 65% bilayers. By contrast, for the graphene prepared using pure Cu films within a slit reactor containing a Ni cover (denoted as Ni cover), the cumulative count plots of the (c) I_{2D}/I_G ratios and (d) FWHM of the 2D band indicated that the produced graphene had a monolayer content of >90%.

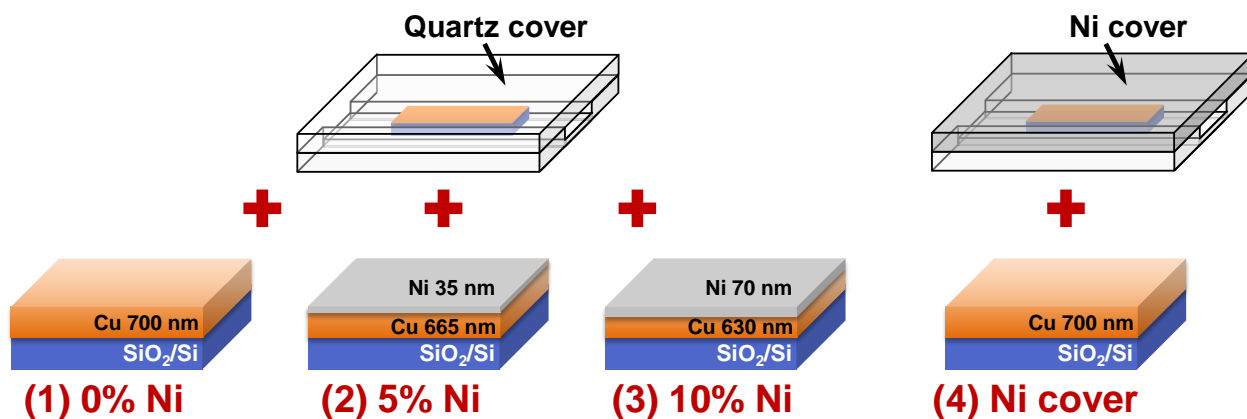


Figure S7. Illustration of four types of metal/SiO₂/Si substrates utilized in this study: (1) deposited pure Cu films with a thickness of 700 nm, denoted as 0% Ni, (2) deposited metal films composed of 650-nm thick Cu (lower layer) and 35-nm-thick Ni (top layer), denoted as 5% Ni, (3) deposited metal films composed of 630-nm-thick Cu (lower layer) and 70-nm-thick Ni (top layer), denoted as 10% Ni; all of the aforementioned three types of substrates were located within a pure quartz slit reactor, and (4) 700-nm-thick pure Cu films within a slit reactor whose quartz cover was replaced by a Ni plate, denoted as Ni cover.

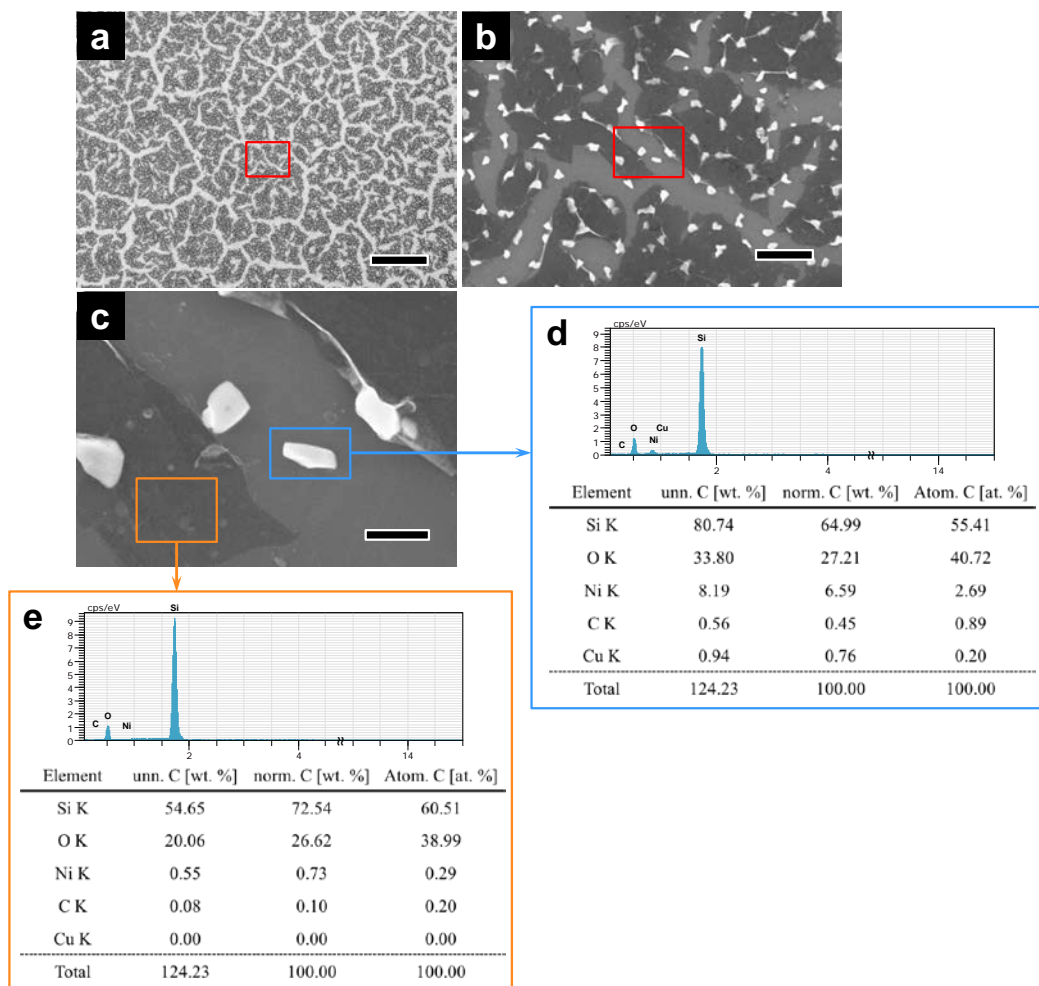


Figure S8. A representative transfer-free graphene prepared using deposited metal films composed of 630-nm-thick Cu (lower layer) and 70-nm-thick Ni (top layer) was examined by SEM under three magnifications: (a) 700 \times , scale bar = 25 μ m; (b) 7000 \times , scale bar = 2 μ m; and (c) 40 000 \times , scale bar = 500 nm. The obtained SEM images indicated that the produced graphene (darkest contrast) was covered by evenly distributed nanoparticles (brightest contrast). The graphene surface and nanoparticles were analyzed with energy-dispersive X-ray spectroscopy (EDS). The EDS examination indicated that (d) the nanoparticles were composed of Cu and Ni (signals of Si and O were from the SiO₂/Si substrate) and that (e) the graphene surface comprised a larger amount of Ni residue than Cu residue.

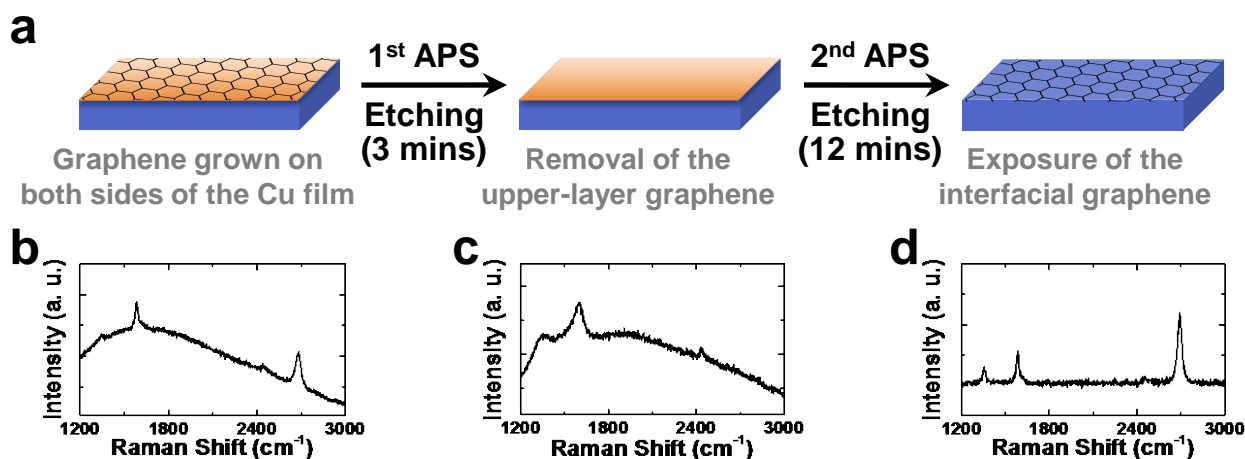


Figure S9. The Cu/SiO₂/Si substrate undergoing a complete CVD process was analyzed with Raman measurement at each step of the Cu removal process. (a) Schematic of the two-step etching process utilized to remove the deposited Cu film. (b) Before etching, the Raman analysis indicated that there were graphene films grown on the top surface of the deposited Cu film. (c) After the first etching step of about 3 mins, the outermost surface of Cu along with the graphene film grown on the upper Cu surface were removed, demonstrated by the disappearance of the 2D band in the recorded Raman spectrum. (d) After the complete removal of the deposited Cu film by the second etching step, the transfer-free graphene grown at the Cu–SiO₂ interface was exposed to show well-characterized G and 2D bands. All of the Raman spectra were determined by the point measurement of at least 5 different locations over a 1 × 1-cm² substrate.

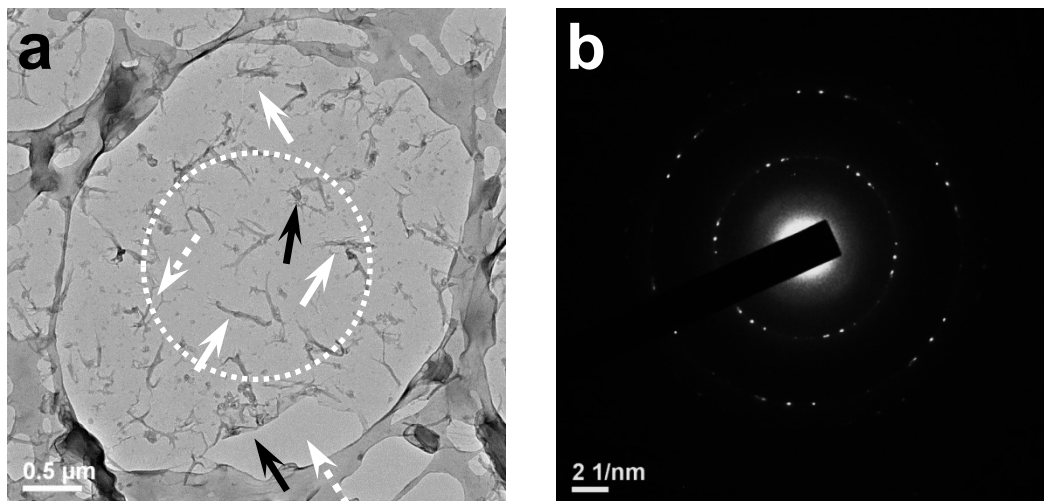


Figure S10. (a) Bright-field TEM image of a transfer-free graphene grown directly on a SiO₂/Si substrate. For TEM examination, the transfer-free graphene was transferred onto a lacey-carbon-coated TEM grid through a conventional polymer-assisted procedure using poly(methyl methacrylate) (PMMA) as the support layer and 40% KOH as the etchant to detach the PMMA/graphene film from the surface of the SiO₂/Si substrate. (b) The selected area electron diffraction (SAED) pattern was recorded from the area defined by the white dashed circle shown in (a). The SAED pattern displayed a typical hexagonal crystalline structure of graphene. The multiple sets of SAED patterns observed in (b) were obtained due to random twisting angles or disoriented stacking order of graphene caused by ripples (a, white solid arrows), tears (a, white dashed arrow), and folds (a, black solid arrow).

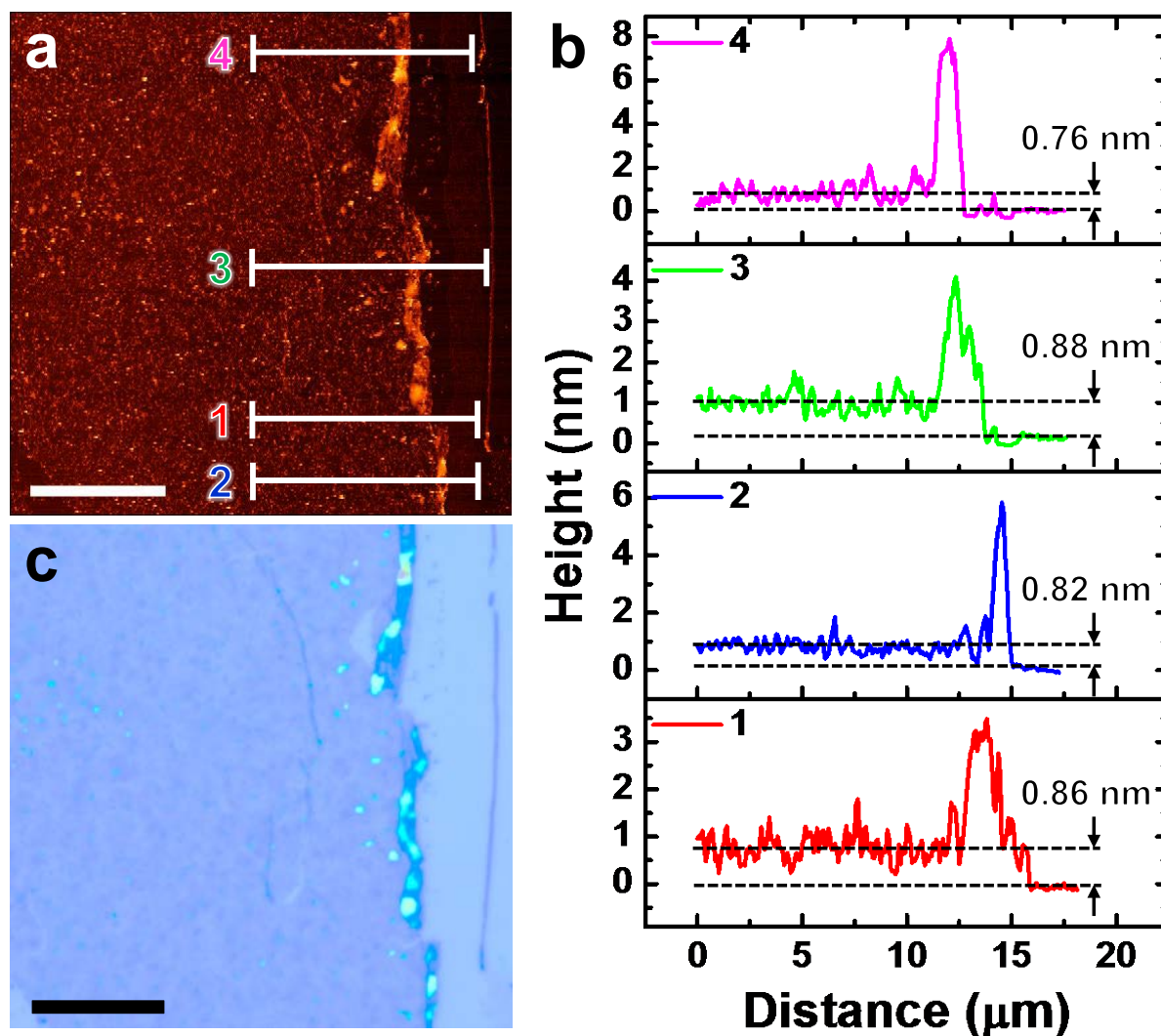


Figure S11. The transfer-free graphene prepared with the optimal synthesis parameters (P37 in Table S2) was characterized by atomic force microscopy (AFM) and optical microscopy. (a) The AFM image shows excellent consistency with the (c) optical microscopic image, on both of which folds of the transfer-free graphene induced by the imperfect etching process of Cu were observed at the edge of the $1 \times 1\text{-cm}^2$ Si substrate. Scale bars: $10 \mu\text{m}$. (b) Line profiles of the height recorded at four different locations marked in (a) demonstrated that the produced graphene with a thickness of about $0.83 \pm 0.05 \text{ nm}$, consistent with the monolayer characteristic of graphene on SiO_2/Si substrates.

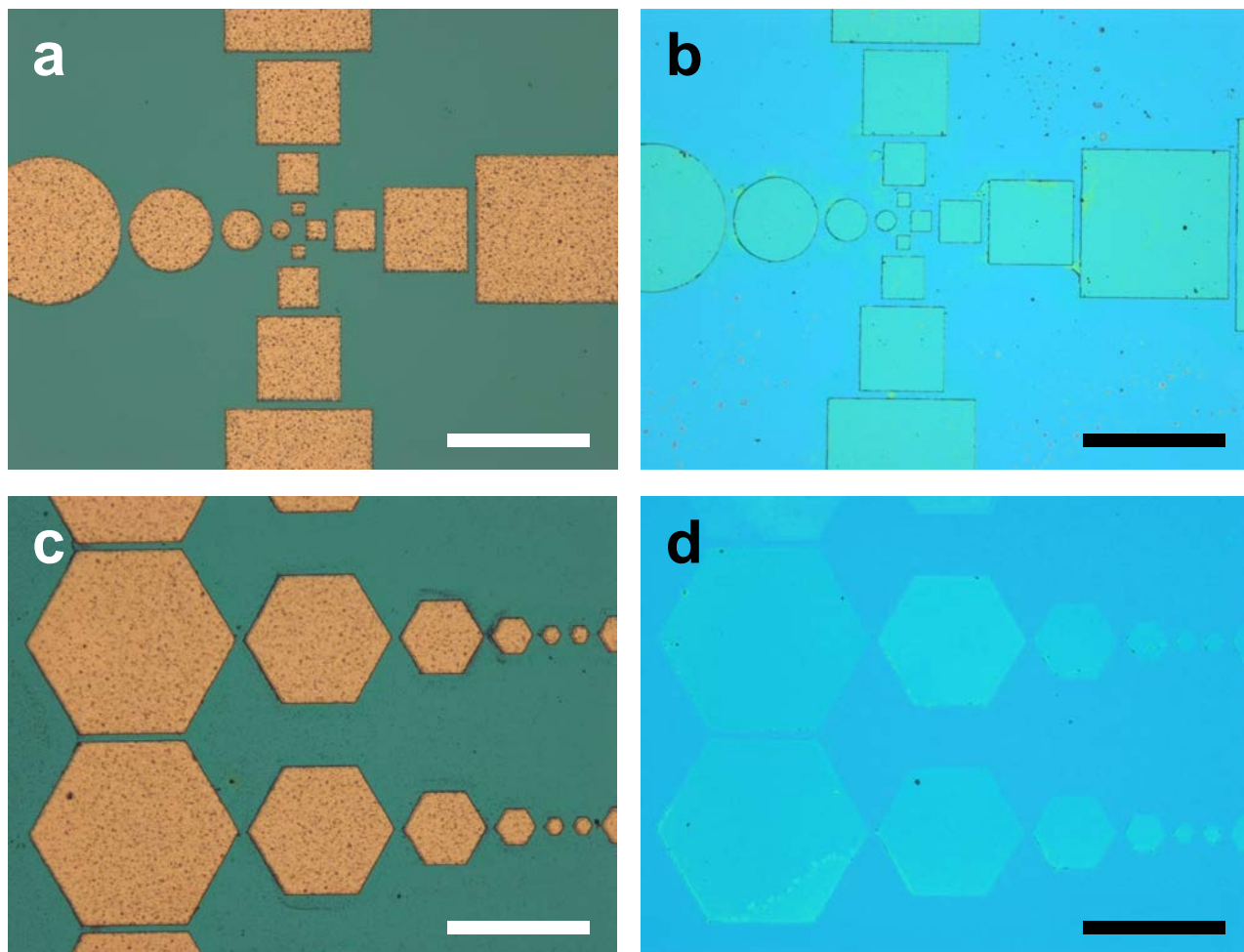


Figure S12. Optical micrographs of (a, c) a patterned Cu film fabricated on a SiO_2/Si substrate by a conventional photolithography process and (b, d) transfer-free graphene patterns obtained with the optimal synthesis protocol (Table S2, P38) using the patterned Cu film depicted in (a) and (c), respectively. Scale bars: 200 μm .

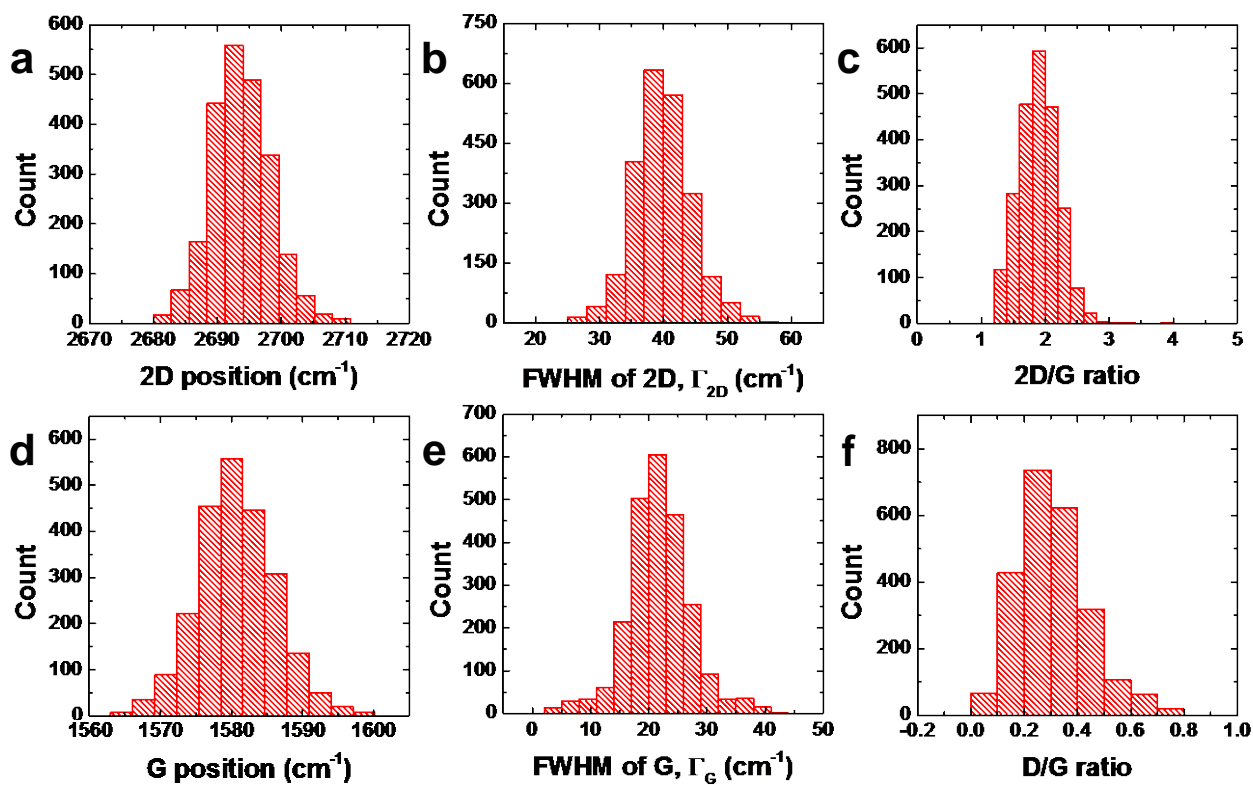


Figure S13. Raman mapping of a representative graphene square with a 60- μm edge was performed to obtain >2000 spectra. The statistical analysis results for these spectra are illustrated as histograms, which indicate that the (a) 2D peak was at $2694.5 \pm 4.6 \text{ cm}^{-1}$, (b) FWHM of the 2D band was $39.3 \pm 2.78 \text{ cm}^{-1}$, (c) I_{2D}/I_G ratio was 1.90 ± 0.32 , (d) G peak was at $1581.3 \pm 6.1 \text{ cm}^{-1}$, (e) FWHM of the G band was $21.7 \pm 1.3 \text{ cm}^{-1}$, and (f) I_D/I_G ratio was 0.31 ± 0.09 .

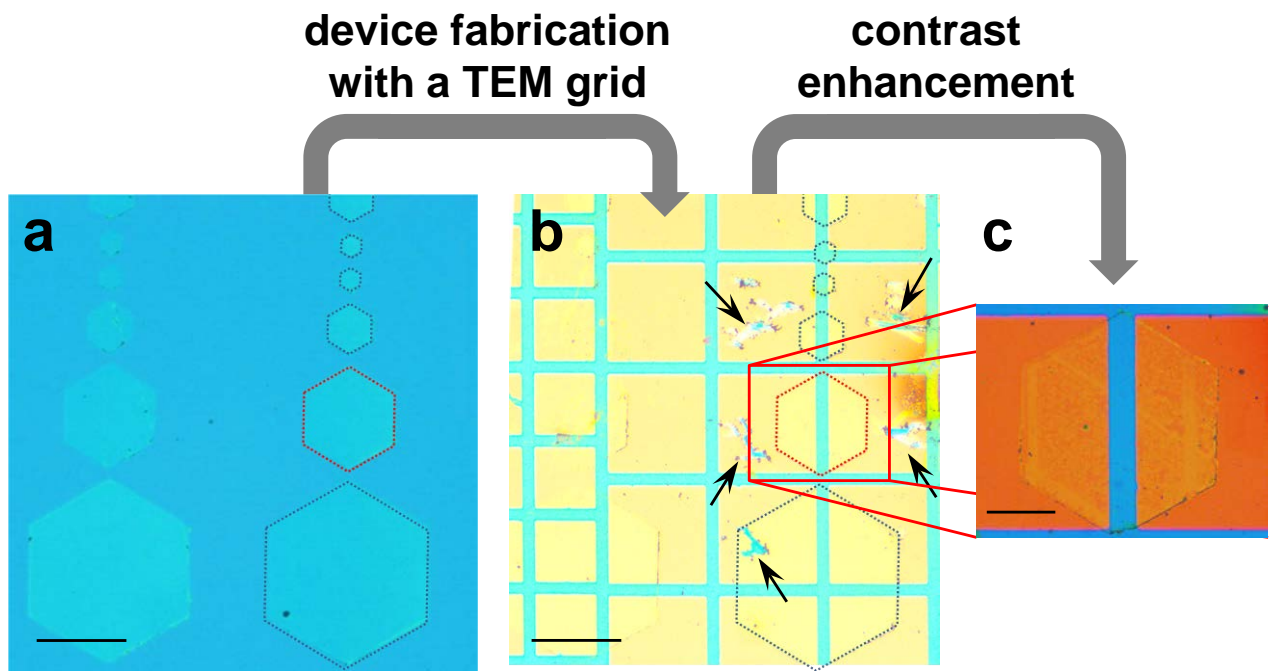


Figure S14. (a) Hexagonal transfer-free graphene patterns prepared with the optimal synthesis protocol (P38 in Table S2). (b) Metal contacts were deposited over the hexagonal transfer-free graphene patterns via thermal evaporation of 10 nm-thick Cr and 50 nm-thick Au using TEM grids as the shadow mask. Scratches and breakage on the metal contacts indicated by black arrows were produced during the electrical measurement using a probe station with sharp probe tips, which must physically contact with the metal pads to apply voltages and thus resulted in damage on the metal pads. (c) The contrast-enhanced optical micrograph of a representative GFET obtained by appropriately adjusting imaging parameters of the CCD camera. Scale bars: (a, b) 100 μm , (c) 35 μm .

REFERENCE

- S1. Ferrari, A. C.; Robertson, J. Interpretation of Raman Spectra of Disordered and Amorphous Carbon. *Phys. Rev. B* **2000**, *61*, 14095–14107.
- S2. Ferrari, A. C.; Robertson, J.; Ferrari, A. C.; Robertson, J. Raman Spectroscopy of Amorphous, Nanostructured, Diamond-Like Carbon, and Nanodiamond. *Philos. Trans. R. Soc. A* **2004**, *362*, 2477–2512.
- S3. Kulkarni, D. D.; Rykaczewski, K.; Singamaneni, S.; Kim, S.; Fedorov, A. G.; Tsukruk, V. V. Thermally Induced Transformations of Amorphous Carbon Nanostructures Fabricated by Electron Beam Induced Deposition. *ACS Appl. Mater. Interfaces* **2011**, *3*, 710–720.
- S4. Kwak, J.; Chu, J. H.; Choi, J.-K.; Park, S.-D.; Go, H.; Kim, S. Y.; Park, K.; Kim, S.-D.; Kim, Y.-W.; Yoon, E.; Kodambaka, S.; Kwon, S.-Y. Near Room-Temperature Synthesis of Transfer-Free Graphene Films. *Nat. Commun.* **2012**, *3*, 645.
- S5. Liu, W.; Li, H.; Xu, C.; Khatami, Y.; Banerjee, K. Synthesis of High-Quality Monolayer and Bilayer Graphene on Copper Using Chemical Vapor Deposition. *Carbon* **2011**, *49*, 4122–4130.
- S6. Kim, W.-J.; Debnath, P. C.; Lee, J.; Lee, J. H.; Lim, D.-S.; Song, Y.-W. Transfer-Free Synthesis of Multilayer Graphene Using a Single-Step Process in an Evaporator and Formation Confirmation by Laser Mode-Locking. *Nanotechnology* **2013**, *24*, 365603.
- S7. Baek, J.; Lee, M.; Kim, J.; Lee, J.; Jeon, S. Transfer-Free Growth of Polymer-Derived Graphene on Dielectric Substrate from Mobile Hot-Wire-Assisted Dual Heating System. *Carbon* **2018**, *127*, 41–46.
- S8. Fauzi, F. B.; Ismail, E.; Ani, M. H.; Syed Abu Bakar, S. N.; Mohamed, M. A.; Majlis, B. Y.; Md Din, M. F.; Azam Mohd Abid, M. A. A Critical Review of the Effects of Fluid Dynamics on Graphene Growth in Atmospheric Pressure Chemical Vapor Deposition. *J. Mater. Res.* **2018**, *33*, 1088–1108.
- S9. Chen, C.-C.; Kuo, C.-J.; Liao, C.-D.; Chang, C.-F.; Tseng, C.-A.; Liu, C.-R.; Chen, Y.-T. Growth of Large-Area Graphene Single Crystals in Confined Reaction Space with

- Diffusion-Driven Chemical Vapor Deposition. *Chem. Mater.* **2015**, *27*, 6249–6258.
- S10. Ramos, W. T. S.; Cunha, T. H. R.; Barcelos, I. D.; Miquita, D. R.; Ferrari, G. A.; de Oliveira, S.; Seara, L. M.; Neto, E. G. S.; Ferlauto, A. S.; Lacerda, R. G. The Role of Hydrogen Partial Pressure on the Annealing of Copper Substrates for Graphene CVD Synthesis. *Mater. Res. Express.* **2016**, *3*, 045602.
- S11. Jung, D. H.; Kang, C.; Kim, M.; Cheong, H.; Lee, H.; Lee, J. S. Effects of Hydrogen Partial Pressure in the Annealing Process on Graphene Growth. *J. Phys. Chem. C* **2014**, *118*, 3574–3580.
- S12. Peng, Z.; Yan, Z.; Sun, Z.; Tour, J. M. Direct Growth of Bilayer Graphene on SiO₂ Substrates by Carbon Diffusion through Nickel. *ACS Nano* **2011**, *5*, 8241–8247.
- S13. Xiong, W.; Zhou, Y. S.; Jiang, L. J.; Sarkar, A.; Mahjouri-Samani, M.; Xie, Z. Q.; Gao, Y.; Ianno, N. J.; Jiang, L.; Lu, Y. F. Single-Step Formation of Graphene on Dielectric Surfaces. *Adv. Mater.* **2013**, *25*, 630–634.
- S14. Yan, K.; Peng, H.; Zhou, Y.; Li, H.; Liu, Z. Formation of Bilayer Bernal Graphene: Layer-by-Layer Epitaxy via Chemical Vapor Deposition. *Nano Lett.* **2011**, *11*, 1106–1110.
- S15. Chen, Y.; Meng, L.; Zhao, W.; Liang, Z.; Wu, X.; Nan, H.; Wu, Z.; Huang, S.; Sun, L.; Wang, J.; Ni, Z. Raman Mapping Investigation of Chemical Vapor Deposition-Fabricated Twisted Bilayer Graphene with Irregular Grains. *Phys. Chem. Chem. Phys.* **2014**, *16*, 21682–21687.
- S16. Gustavo Cançado, L.; Gomes da Silva, M.; Martins Ferreira, E. H.; Hof, F.; Kampioti, K.; Huang, K.; Pénicaud, A.; Alberto Achete, C.; Capaz, R. B.; Jorio, A. Disentangling Contributions of Point and Line Defects in the Raman Spectra of Graphene-Related Materials. *2D Mater.* **2017**, *4*, 025039.
- S17. Martins Ferreira, E. H.; Moutinho, M. V. O.; Stavale, F.; Lucchese, M. M.; Capaz, R. B.; Achete, C. A.; Jorio, A. Evolution of the Raman Spectra from Single-, Few-, and Many-Layer Graphene with Increasing Disorder. *Phys. Rev. B* **2010**, *82*, 125429.
- S18. Shin, Y. Y.; Lozada-Hidalgo, M.; Sambricio, J. L.; Grigorieva, I. V.; Geim, A. K.; Casiraghi,

- C. Raman Spectroscopy of Highly Pressurized Graphene Membranes. *Appl. Phys. Lett.* **2016**, *108*, 221907.
- S19. Wang, Y. y.; Ni, Z. h.; Yu, T.; Shen, Z. X.; Wang, H. m.; Wu, Y. h.; Chen, W.; Shen Wee, A. T. Raman Studies of Monolayer Graphene: The Substrate Effect. *J. Phys. Chem. C* **2008**, *112*, 10637–10640.
- S20. Kim, S.; Nah, J.; Jo, I.; Shahrjerdi, D.; Colombo, L.; Yao, Z.; Tutuc, E.; Banerjee, S. K. Realization of a High Mobility Dual-Gated Graphene Field-Effect Transistor with Al₂O₃ Dielectric. *Appl. Phys. Lett.* **2009**, *94*, 062107.
- S21. Liao, L.; Bai, J.; Qu, Y.; Lin, Y.-C.; Li, Y.; Huang, Y.; Duan, X. High- κ Oxide Nanoribbons as Gate Dielectrics for High Mobility Top-Gated Graphene Transistors. *Proc. Natl. Acad. Sci. USA* **2010**, *107*, 6711–6715.